# HELICON PLASMA SOURCES

Francis F. Chen

Electrical Engineering Department

PPG- 1506 January, 1994

To be published as a chapter in *High Density Plasma Sources*, ed. by Oleg A. Popov (Noyes).

# TABLE OF CONTENTS

# HELICON PLASMA SOURCES

**FRANCIS F. CHEN**
University of California, Los Angeles

## 1.0 INTRODUCTION

### 1.1 Brief history

Low-frequency whistler waves are well known in ionospheric research because of their insensitivity to variations in plasma density and magnetic field. When these waves are confined to a cylinder, they lose their electromagnetic character and become partly electrostatic, changing their propagation and polarization characteristics as well. These bounded whistlers, called helicons, were first investigated and observed in solid state plasmas (2, 17, 52, 75). Upon the discovery by Lehane and Thonemann (64) in England that helicons can exist in a gaseous plasma, a series of theoretical papers (60, 5, 6, 7, 49, 42, 41), following a general formulation for waves in cylinders by Woods (89, 90), laid the foundation for helicon research. Experiments were resumed in Australia by Davies and Christiansen (42) and Boswell (8). Interest in this academic subject subsided until Boswell (16, 9, 10) found that helicon waves were unusually efficient in producing plasmas; in fact, the absorption of rf energy was more than 1000 times faster than the theoretical rate due to collisions. In 1985, Chen (23) proposed Landau damping as the reason for this discrepancy. The complete calculation appeared in 1991 (27), together with the suggestion that wave acceleration by the Landau mechanism can be used to produce primary electrons at the optimum energy for ionization. Since 1985, a number of papers have been written to verify the collisionless damping mechanism (61, 68, 92, 32, 34), to clarify the physics of helicon discharges (77, 78, 79, 55, 56, 34, 21, 82, 83, 85), to explore the possibilities of helicon sources (24, 15, 25, 26, 91, 14, 68, 33, 35, 37), and to test their worth in manufacturing applications (13, 73, 20, 74, 80, 81, 19, 18, 70, 54, 59). In the period 1986-1992, the main groups engaged in helicon research were Boswell et al. (8, 13, 14, 15, 20, 68, 73, 74, 91, 92), Chen et al. (25, 26, 27, 24, 32, 33, 34, 35, 37, 43, 85), and Shoji et al. (19, 18, 54, 55, 56, 61, 70, 77, 78, 79, 80, 81, 82). By 1993, the

helicon source had emerged as one of the major alternatives to the RIE (Reactive Ion Etching) discharge for high-throughput plasma-aided manufacturing.

### 1.2 Advantages of helicon sources

To be a viable alternative to the RIE discharge, the ECR (Electron Cyclotron Resonance) source, and the RFI (Radiofrequency Inductive) or TCP (Transformer Coupled Plasma) discharge, the helicon source must be a better practical tool. In contrast to the other plasma sources, helicon discharges started from a solid theoretical background, but their performance in practical use is relatively undocumented. Optimization of the configuration has not yet been extensively investigated, and computer modeling in realistic geometries has only recently begun. The purported advantages of helicon sources are as follows.

**High density.** Typical helicon discharges in argon with 1-2 kW of rf power have average plasma densities in excess of $10^{13}$ $cm^{-3}$ and peak densities of order $10^{14}$ $cm^{-3}$ about two orders of magnitude higher than in usual processing plasmas. However, densities in gases other than argon are considerably lower, the density will drop when spread over a large area, and the quoted power is somewhat higher than normally used. When these factors are taken into account, this advantage of helicon sources is reduced to perhaps a factor of 3-10, which is still an appreciable gain.

**High efficiency.** The fact that helicon discharges produce more plasma at given input power than other rf or dc discharges has been known since the early experiments of Boswell (8, 10). That the density jumps dramatically when the discharge snaps from a nonresonant rf discharge into the helicon mode has been seen by Boswell (10), by Chen (25), and by Shoji (82). The key to the helicons' efficiency is the acceleration of electrons to ionizing energies by "surfing" on the wave, leading to rapid transfer of wave energy to primary electrons.

**Finite but low magnetic field.** Ionization efficiency is a matter of conserving the primary electrons. The RIE and RFI sources have no magnetic field in the source region, and hence the primaries are confined only by electrostatic sheath fields. Helicon sources employ the principle of the Penning discharge in using a magnetic field to confine electrons in the radial direction. Compared with the 875 G needed for the ECR source, however, the helicon source can be operated at 100-300 G, sufficient for trapping the

electrons but not the ions. There is also a possibility of a low-field mode of the helicon discharge (32, 43) which requires only 10-40 G. A second important benefit of a magnetic field is the increased skin depth. At high pressures, the penetration length of rf fields depends on the collision frequency; but at low pressures, this length approaches the collisionless skin depth $c/\omega_p$, or an anomalous value somewhat larger than this. When a magnetic field prevents electrons from moving in such a direction as to shield out the applied electric field, however, it is the ions that must do the shielding, and the skin depth is increased to the order of $c/\Omega_p$, where $\Omega_p$ is the ion plasma frequency.

**No internal electrodes.** Since the antenna lies outside the vacuum chamber, the possibility of contamination or sputtering from the electrodes producing the plasma is eliminated. Freedom in the choice of wall material exposed to the plasma also allows control of the release of oxygen, which is useful for passivation of the etching process. These advantages are shared to some extent by the RFI and ECR discharges.

**Uniformity and quiescence.** Though the factors that affect density uniformity are not completely understood, plasmas that are uniform over a large fraction of their radii have been reported both for the m = 0 mode (19, 18) and the m = 1 mode (34), even in the source region. Since the helicon is a "remote" source, in which the processing can be done after the plasma has been spread over a large area, control of uniformity may be easier than for the RIE or RFI sources. The plasma is also free from low-frequency fluctuations as long as the helicon resonance is struck. Transition between resonant and non-resonant discharges can result in relaxation oscillations (25). Oscillations in the drift-wave frequency range are occasionally seen, but these can be controlled by shaping the magnetic field (37).

**Low pressure operation.** In etching applications, it is important to operate at pressures in the 10 mTorr range or below, so that the ions impinge on the wafer through a collisionless sheath. Because the Landau damping mechanism does not require collisions, the helicon source is well suited for low-pressure operation.

**Independent control of ion energy.** In the RIE discharge, the density can be increased only by increasing the rf power and causing the sheath drop to oscillate violently in each rf cycle. The ion energy therefore is not constant and not independently controllable. In remote sources such as the helicon, the sheath drop is not necessarily related to the rf power and does not oscillate with large amplitude during the rf cycle.

The ion energy can, in principle, be set to a reasonably small value by applying an rf bias to the wafer, or by the self-bias mechanism described below. Few measurements of ion energies are available; Giapis et al. (50) have measured energies of metastable ions, and Charles (21) has measured ion velocities in a "helicon" source without magnetic field.

**Control of electron energies.** Since the phase velocity of helicon waves can be controlled by the frequency and antenna length, the energy of the electrons accelerated by the wave can be adjusted. This gives a degree of control over the electron energy distribution, and therefore the production of different molecular species. The change in distribution function with varying plasma parameters has been seen by Zhu and Boswell (92), Loewenhardt et al. (68), and Shoji et al. (80).

**Remote operation.** The plasma can be transported from the source to a region with no magnetic fields or with only surface fields. Processing done in such a region is less subject to plasma nonuniformities and to electric fields that can cause damage to semiconductor devices.

**Good access at ends.** Since the antenna surrounds the vacuum tube, there are no electrodes to interfere with particle or light beams directed along the tube. This feature makes the helicon source suitable for applications to plasma accelerators or generators of coherent radiation. If enough power is available, a dense plasma of arbitrary length can be made with periodic antenna arrays.

**Self-applied dc bias.** Fast electrons accelerated by the helicon wave has been found to charge a floating plate to potentials higher than -200 V (32). This potential can be controlled by changing the distance between the plate and the antenna. Thus, a negative dc potential can be applied to a wafer without using a separate rf power supply.

**Powerful current drive.** With proper design, the Landau mechanism can trap and accelerate a large number of electrons. The helicon source could be made into a very efficient dc generator of electron beams with high current density.

Helicon sources have a number of features which can be exploited for different applications. Extensive experimentation is needed to see whether these purported advantages can be realized.

## 2.0 SUMMARY OF THEORY

### 2.1 Helicon waves in uniform plasmas

**Fundamental equations.** The governing equations with damping but neglecting ion motions and displacement current have been treated extensively by Klozenberg et al. (60):

Eq. (1) $$m\frac{\partial \mathbf{v}}{\partial t} = -e(\mathbf{E} + \mathbf{v} \times \mathbf{B}_0) - m\nu\mathbf{v}$$

Eq. (2) $$\nabla \times \mathbf{E} = -\dot{\mathbf{B}}$$

Eq. (3) $$\nabla \times \mathbf{B} = \mu_0 \mathbf{j}$$

Eq. (4) $$\mathbf{j} = -en_0\mathbf{v}.$$

Here $\mathbf{B}_0$ is the dc magnetic field in the $z$ direction; $\mathbf{v}$ is the wave velocity of the cold electron fluid of density $n_0$; $\nu$ is a phenomenological collision frequency, and $\mathbf{E}$, $\mathbf{B}$, and $\mathbf{j}$ the oscillating quantities in Maxwell's equations. The resistivity $\eta$ is given by

Eq. (5) $$\eta = \frac{m\nu}{n_0 e^2}.$$

For waves of the form $exp[i(kz - \omega t)]$, Eqs. (1), (4), and (5) give

Eq. (6) $$\mathbf{E} = \frac{1}{en_0}(\mathbf{j} \times \mathbf{B}_0) + \eta\left(1 - \frac{i\omega}{\nu}\right)\mathbf{j}.$$

Using $\mathbf{E}$ and $\mathbf{j}$ from Eqs. (2) and (3), this equation can be written

Eq. (7) $$(\omega + i\nu)\nabla \times \nabla \times \mathbf{B} - k\omega_c \nabla \times \mathbf{B} + (\omega\omega_p^2/c^2)\mathbf{B} = 0,$$

where the cyclotron and plasma frequencies are given by

Eq. (8) $$\omega_c \equiv eB_0/m \quad \text{and} \quad \omega_p^2 \equiv n_0 e^2/\varepsilon_0 m.$$

Eq. (7) can be factored into

Eq. (9) $$(\beta_1 - \nabla\times)(\beta_2 - \nabla\times)\mathbf{B} = 0,$$

where $\beta_1$ and $\beta_2$ are the roots of the algebraic equation

Eq. (10) $$(\omega + i\nu)\beta^2 - k\omega_c\beta + \omega\omega_p{}^2/c^2 = 0.$$

The most general solution **B** is the sum of $\mathbf{B}_1$ and $\mathbf{B}_2$, which satisfy

Eq. (11) $$\nabla\times\mathbf{B}_1 = \beta_1\mathbf{B}_1, \qquad \nabla\times\mathbf{B}_2 = \beta_2\mathbf{B}_2.$$

Though solutions which are coupled by a common boundary condition at $r = a$ are possible (26), we consider here only those solutions which separately satisfy the boundary condition. Thus, after taking the curl of Eq. (11), we have two distinct waves, each satisfying

Eq. (12) $$\nabla^2\mathbf{B}_j + \beta_j{}^2\mathbf{B}_j = 0, \qquad j = 1, 2.$$

For uniform plasmas, we can define the constants $\alpha$ and $\gamma$ as follows:

Eq. (13) $$\alpha \equiv \frac{\omega}{k}\frac{\omega_p{}^2}{\omega_c c^2} = \frac{\omega}{k}\frac{n_0 e\mu_0}{B_0}, \qquad \gamma \equiv \frac{\omega + i\nu}{\omega_c},$$

so that the solutions of Eq. (10) can be written

Eq. (14) $$\beta_{1,2} = \frac{k}{2\gamma}\left[1 \mp \left(1 - \frac{4\alpha\gamma}{k}\right)^{1/2}\right].$$

For $\omega/\omega_c$ so small that $\gamma << k/4\alpha$, the roots $\beta_j$ have the approximate values

Eq. (15) $$\beta_1 \cong \alpha\left(1 + \frac{\alpha\gamma}{k}\right) \cong \alpha$$

Eq. (16)
$$\beta_2 \cong \frac{k}{\gamma} - \alpha \cong \frac{k\omega_c}{\omega}.$$

When the damping term is neglected, the classical helicon wave is given by $\beta_1 = \alpha$; the helicon-ECR wave treated later is given by $\beta_2$. For now, we consider that $\omega/\omega_c$ is so small that only one root $\beta$ exists.

**Dispersion relation.** For the standard helicon wave, Eq. (12) becomes

Eq. (17)
$$\nabla^2 \mathbf{B} + \beta^2 \mathbf{B} = 0,$$

with $\beta \cong \alpha$. The *r* and *6* components of this vector Helmholtz equation both contain $B_r$ and $B_\theta$, but the equation can be separated by expressing **B** in rotating coordinates. For

$$\mathbf{B} = \mathbf{B}(r) exp[i(m\theta + kz - \omega t)],$$

the right- and left-hand rotating components $B_R$ and $B_L$ are defined by

Eq. (18)
$$B_R = (B_r - iB_\theta)/\sqrt{2}, \qquad B_L = (B_r + iB_\theta)/\sqrt{2}.$$

In terms of these variables, the components of Eq. (17) are

Eq. (19)
$$\left\{\frac{\partial^2}{\partial\rho^2} + \frac{1}{\rho}\frac{\partial}{\partial\rho} + \left[1 - \frac{(m-1)^2}{\rho^2}\right]\right\} B_R = 0$$
$$\left\{\frac{\partial^2}{\partial\rho^2} + \frac{1}{\rho}\frac{\partial}{\partial\rho} + \left[1 - \frac{(m+1)^2}{\rho^2}\right]\right\} B_L = 0$$
$$\left\{\frac{\partial^2}{\partial\rho^2} + \frac{1}{\rho}\frac{\partial}{\partial\rho} + \left[1 - \frac{m^2}{\rho^2}\right]\right\} B_z = 0$$

where

Eq. (20)
$$\rho \equiv Tr, \qquad T^2 \equiv \beta^2 - k^2.$$

Since Eqs. (19) are Bessel's equations, the components of **B** are given by

Eq. (21) $$B_R = C_1 J_{m-1}(Tr), \quad B_L = C_2 J_{m+1}(Tr), \quad B_z = C_3 J_m(Tr).$$

Two of the coefficients $C_j$ can be eliminated in favor of a single wave amplitude by using $\nabla \cdot \mathbf{B} = 0$ and the first-order equation Eq. (11). In the absence of damping we then find (27)

Eq. (22)
$$\begin{aligned} B_r &= A\left[(\beta+k)J_{m-1} + (\beta-k)J_{m+1}\right] \\ B_\theta &= iA\left[(\beta+k)J_{m-1} - (\beta-k)J_{m+1}\right] \\ B_z &= -2iTAJ_m \end{aligned}$$

The components of E can be found from Eq. (2):

Eq. (23)
$$\begin{aligned} E_r &= i(\omega/k)A\left[(\beta+k)J_{m-1} - (\beta-k)J_{m+1}\right] \\ E_\theta &= -(\omega/k)A\left[(\beta+k)J_{m-1} + (\beta-k)J_{m+1}\right] \\ E_z &= 0, \end{aligned}$$

the last equation being a consequence of Eq. (6) when there is no damping.

The boundary condition for an insulating wall at $r = a$ is $j_r = 0$. From Eqs. (3) and (11), we see that

Eq. (24) $$\mathbf{j} = (\beta/\mu_0)\mathbf{B}.$$

Hence, $B_r(a) = 0$. For a conducting cylinder, we require $E_\theta(a) = 0$; and Eq. (2) gives $B_r(a) = 0$ for this case also. From Eq.(22), we then have

Eq. (25) $$(\beta+k)J_{m-1}(Ta) + (\beta-k)J_{m+1}(Ta) = 0,$$

or, equivalently,

Eq. (26) $$m\beta J_m(Ta) + ka\,J_m'(Ta) = 0,$$

where $T^2 = \beta^2 + k^2$ and the prime (') indicates $\partial/\partial r$. Though Eq. (14) indicates the possibility of two values of $\beta$ for given k, $\alpha$, and $\gamma$ (corresponding to given frequency,

wavelength, density, and magnetic field, only one value of β will satisfy the boundary condition Eq. (25) or Eq. (26). Using Eq. (13), we can write Eq. (10) as

Eq. (27) $$\gamma\beta^2 - k\beta + k\alpha = 0.$$

Eq. (25) can be iterated to find eigenvalues β for various radial modes. The classical helicon wave is given by the limit of small γ, so that $\alpha \approx \beta$, and α is a constant depending on the value of β. We see from Eq. (13) that this implies that density ($n_0$) is proportional to magnetic field ($B_0$), for given phase velocity ω/k. Because of Landau damping, this phase velocity will be related to the energy of the fast electrons accelerated by the wave; consequently, it is convenient to plot the dispersion relation not as ω vs. k, but as $n_0$ vs. $B_0$ for given ω/k. An example of such a relation is given in Fig. 1 for the lowest radial mode with azimuthal mode numbers m = -1, 0, and +1.

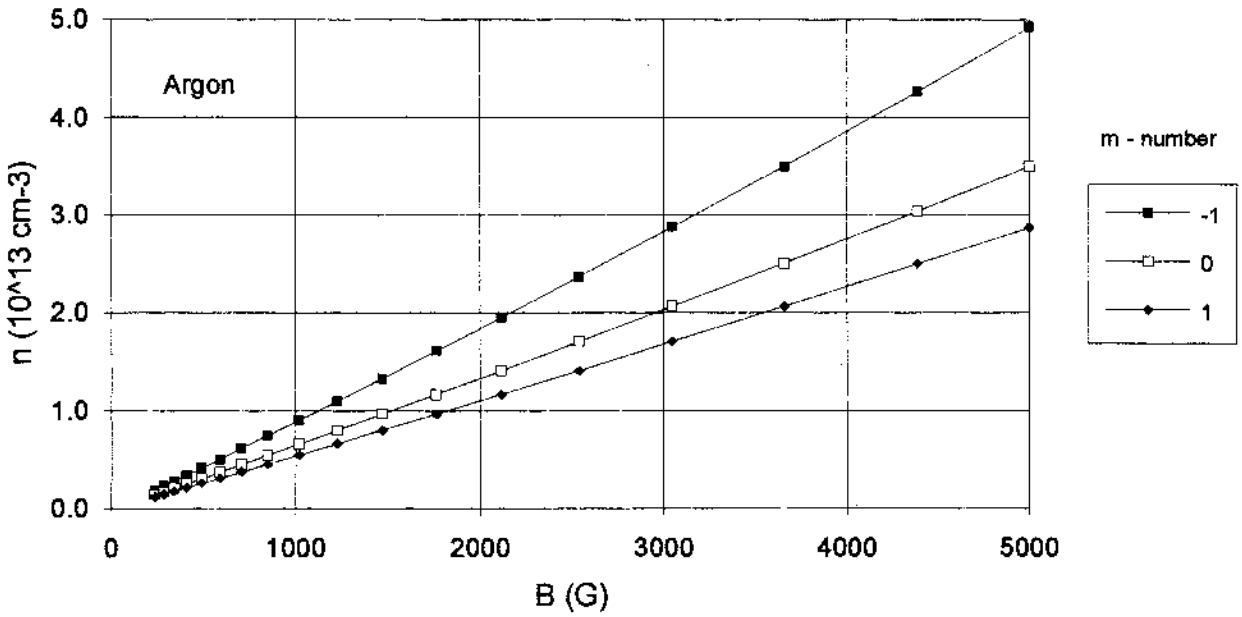


**Figure 1.** Dispersion relation for undamped helicon waves in argon. The resonant density is given in units of $10^{13}$ $cm^{-3}$ vs. the magnetic field in gauss. The curves are for the lowest radial mode and for the three lowest azimuthal modes in a cylinder of 5 cm radius. The wavelength of 44 cm at a frequency of 13.56 MHz has been chosen to give a phase velocity equal to the velocity of 100-eV electrons.

**Wave patterns.** The field components given in Eqs. (22) and (23) can be used to plot the wave's electric and magnetic field lines, whose transverse components are perpen-

dicular to each other. This is shown in Fig. 2 for the m = -1 and +1 modes. In addition to these components, the magnetic field has a large $B_z$ component, which is required to preserve $\nabla \cdot B = 0$. This is not true for the E-field, which has $E_z \approx 0$. Thus, $\nabla \cdot E \neq 0$, as can be seen in the divergence of the E-lines. Indeed, the associated space charge gives rise to an electrostatic component of E which is its dominant part. It is also seen that the m = -1 mode is more concentrated toward the axis than the m = 1 mode. This difference depends on the value of *ka* and diminishes with decreasing *ka*. Since the fields vary as exp $i(m\theta + kz - \omega t)$, it is clear that the same pattern exists at all *z* but is rotated in *6*, as long as $m \neq 0$.

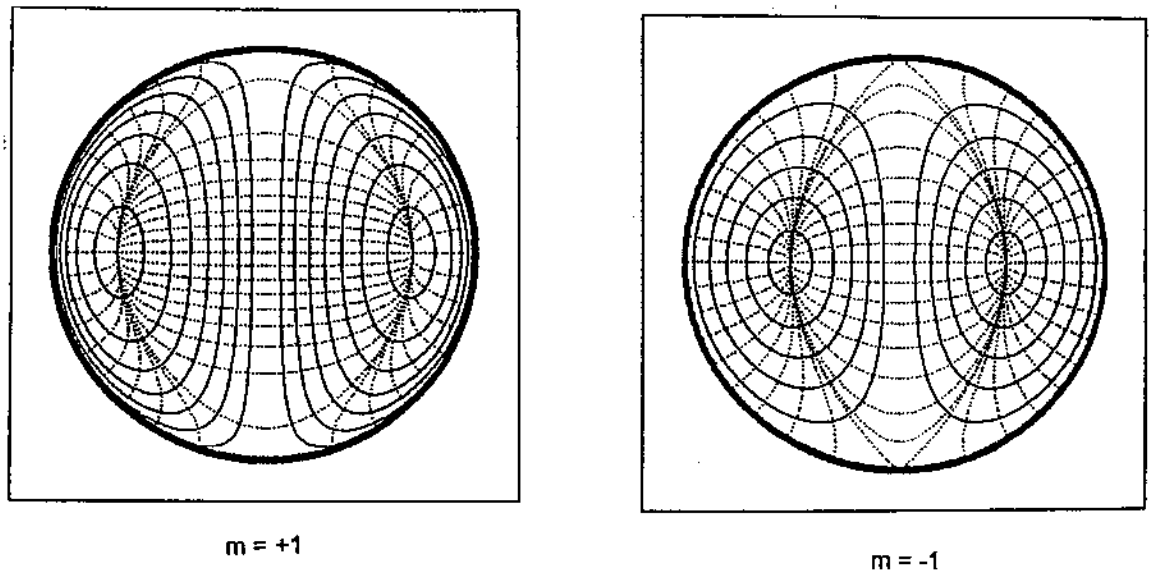


**Figure 2.** Pattern of magnetic (solid) and electric (dashed) field lines in the m = +1 and -1 modes of the helicon wave in a uniform plasma in a plane perpendicular to the dc magnetic field (Ref. 35).

The electric field pattern in space at one instant in time for the m = +1 mode is shown in Fig. 3. If the propagation is in the direction of $\mathbf{B_0}$ ($k > 0$), a stationary observer looking along $\mathbf{B_0}$ will see the pattern rotating clockwise in time; this is the "right-hand" wave. For $k < 0$, this pattern would give the "left-hand" wave. The figure for the m = -1 mode would rotate the opposite way in *z*, so that $k > 0$ would give left-hand polarization, while $k < 0$ would give right-hand polarization. For the m = 0 mode, however, the pattern changes with *z*, as shown in Fig. 4, in such a way that the electric field changes from pure electrostatic to pure electromagnetic at different phases. In long, thin tubes (small *ka*) the E-field is predominantly electrostatic for the major part of each wavelength.

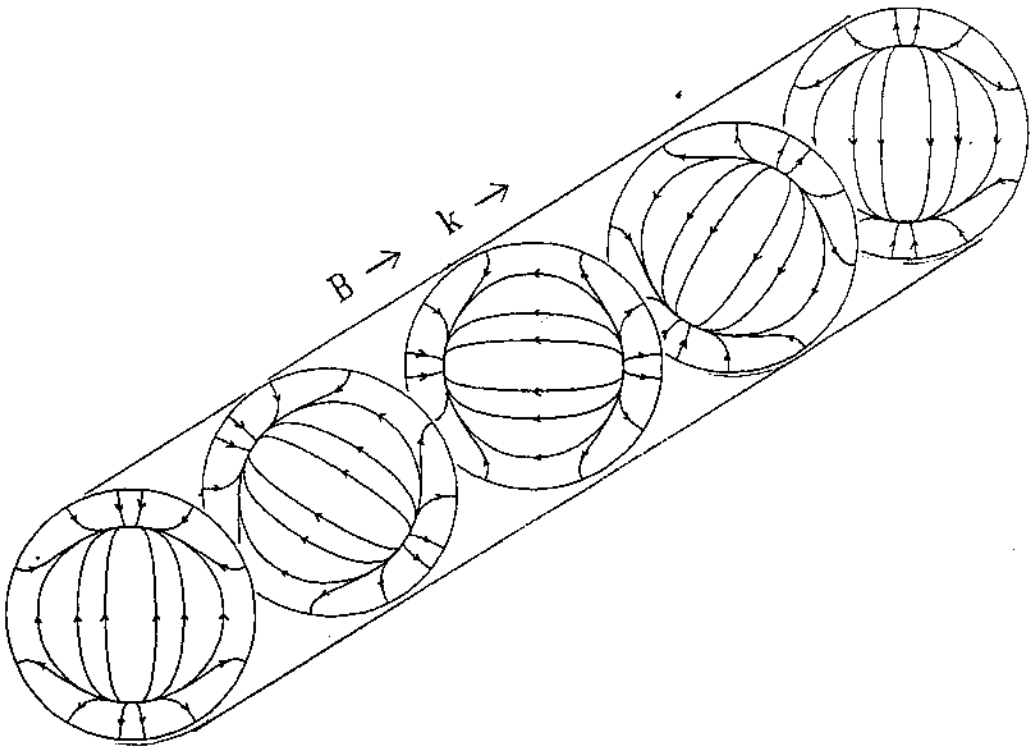


**Figure 3.** Instantaneous electric field pattern for an m = +1 helicon wave in space (Ref. 27).

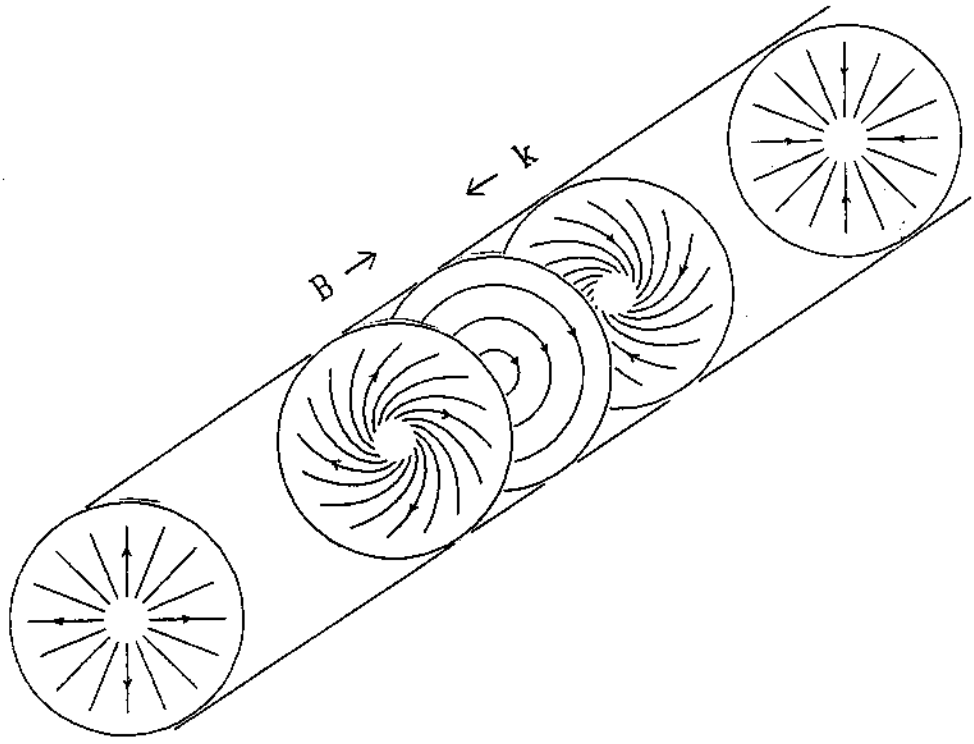


**Figure 4.** Instantaneous electric field pattern for an m = 0 helicon wave in space (Ref. 27).

## 2.2 Other effects

**The helicon-ECR mode.** At very low magnetic fields, the value of $\gamma$ [Eq.(13)] cannot be neglected, and both roots of the quadratic Eq. (27), given by Eq. (14), must be considered. The root $\beta_1 \approx \alpha$ of Eq. (15) is essentially a low-frequency whistler wave propagating at an angle $\theta$ to the magnetic field. The usual dispersion relation is

Eq. (28) $$\frac{c^2 k_{tot}^{\ 2}}{\omega^2} = 1 - \frac{\omega_p^{\ 2}}{\omega(\omega - \omega_c \cos\theta)},$$

where $\cos\theta = k_{||} / k_{tot}$. Identifying $k_{tot}$ with $\beta$ and $k_{||}$ with k, and taking the limit $\omega \rightarrow 0$, we have

Eq. (29) $$\beta^2 = \frac{\omega^2}{c^2} \frac{\omega_p^{\ 2}}{\omega\omega_c (k/\beta)},$$

which is exactly $\beta = \alpha$. The root $\beta_2 \approx k\omega_c/\omega$ is essentially an electron cyclotron wave at an angle $\theta$ to the magnetic field. The usual dispersion relation for this wave is

Eq. (30) $$T^2 = -k^2 \frac{(\omega^2 - \omega_p^{\ 2})(\omega^2 - \omega_c^{\ 2})}{\omega^2(\omega^2 - \omega_p^{\ 2} - \omega_c^{\ 2})}.$$

Identifying $T^2$ with $\beta^2$ and taking the limit $\omega^2 << \omega_c^2 << \omega_p^2$, we obtain

Eq. (31) $$\beta^2 = k^2 \frac{\omega_c^{\ 2}}{\omega^2}\left(1 + \frac{\omega_c^{\ 2}}{\omega_p^{\ 2}}\right)^{-1},$$

which is essentially Eq. (16). Thus, $\beta_2$ is an electron cyclotron wave in finite geometry, which in the electrostatic limit is commonly known as a Trivelpiece-Gould mode. Each of these waves satisfies Eq. (12) with its value of $\beta$. There are two possibilities: either $\mathbf{B_1}$ and $\mathbf{B_2}$ each satisfies the boundary condition $B_r(a) = 0$, or the two modes exist simultaneously in such a way that their radial currents $j_r(a)$ cancel each other on an insulating wall, or their tangential electric fields $E_\theta(a)$ cancel each other on a conducting wall. If each mode satisfies the same boundary condition, then the values of both $\beta_1$ and $\beta_2$ must be the same as that found by solving Eq. (25). The resulting dispersion relation

was shown in Fig. 1. However, since the electron mass is relevant only at low magnetic fields, we show in Fig. 5 the low-field part of Fig. 1. We see that the effect of finite electron mass is to shift the n-B curve downwards, giving rise to a threshold magnetic field below which helicons cannot exist.

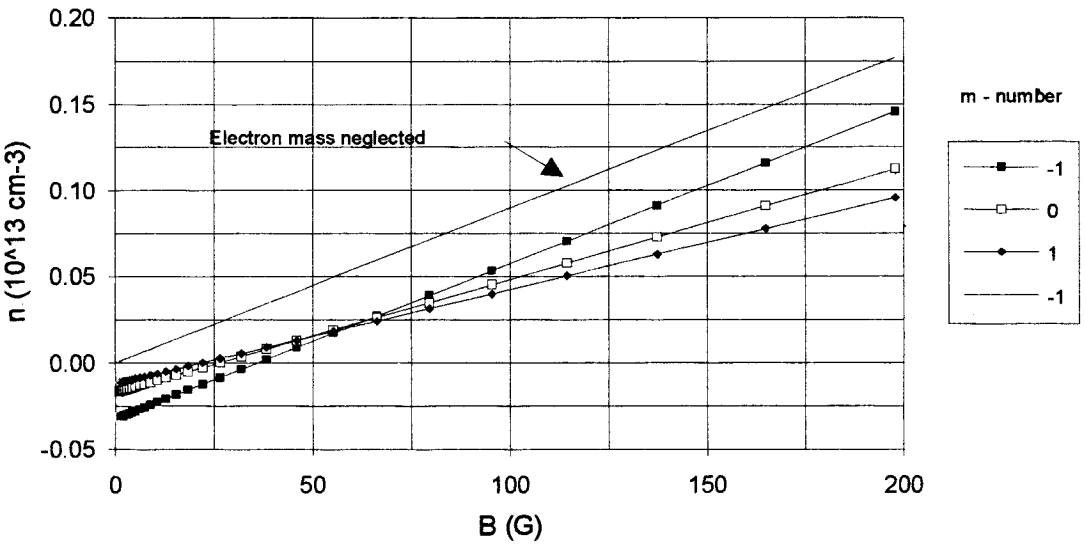


**Figure 5.** Dispersion relation for helicon waves including electron mass. Parameters are the same as in Fig. 1. The line is for the m = -1 mode when the electron mass is neglected.

We now consider the second possibility, which is that both $\mathbf{B_1}$ and $\mathbf{B_2}$ exist at the same time and are coupled by the boundary condition. Let R be the ratio of amplitudes $A_2/A_1$. For an insulating boundary, we require, from Eq. (24),

Eq. (32) $$j_{r1} + R j_{r2} = 0, \qquad \beta_1 B_{r1} + R\beta_2 B_{r2} = 0.$$

For a conducting boundary, we have, from Eqs. (22) and (23),

Eq. (33) $$E_{\theta 1} + R E_{\theta 2} = 0, \qquad B_{r1} + R B_{r2} = 0.$$

If both modes have the same $m$ and $k$, different values of $\beta_1$ and $\beta_2$ can be found for any $n_0$ and $B_0$, and an appropriate (positive or negative) value of R chosen to satisfy the boundary condition. However, $n_0$ and $B_0$ must lie in the range that makes $\beta^2 - \alpha^2 > 0$, and one of the modes must not be a natural mode, as described above, which has $j_r = 0$ by itself.

Interest in the helicon-ECR branch originally arose because of the observation of a density peak by Chen and Decker (32) and Chen and Chevalier (34) occurring at low magnetic fields agreeing approximately with Eq. (31). The n-B curve from a discharge in a 2-cm diameter tube is shown in Fig. 6. However, such a density peak is not predicted by the dispersion relations given above for single or coupled modes. It could be due to other effects,

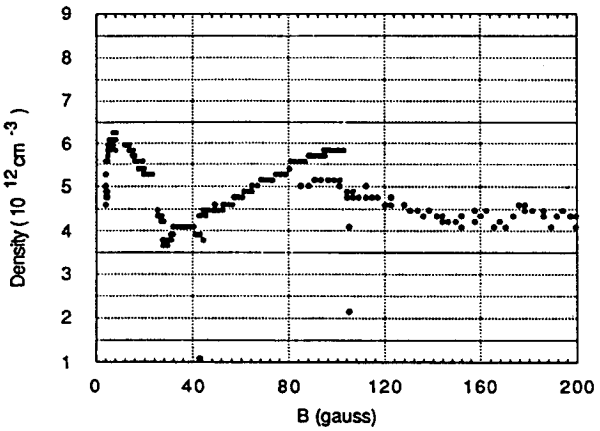


**Figure 6.** Density peak in a helicon discharge at low magnetic fields, from Ref. 32.

such as surface waves, reflections from metal surfaces outside the vacuum chamber, or increased ionization from cyclotron-accelerated electrons. Cyclotron damping of whistler waves in this context was measured by Christopoulos et al. (38) and has recently been treated theoretically by Harvey and Lashmore-Davies (53). On the other hand, Cui and Boswell (39) have obtained evidence, with low rf power, of surface absorption and electron tail formation whenever $\omega \geq \omega_c$ somewhere in the chamber, but not when $\omega < \omega_c$ everywhere. However, no peak in density was observed near cyclotron resonance; in fact, the density decreased from its already low value of $\approx 3 \times 10^9$ cm$^{-3}$.

**Finite ion mass effects.** The motion of the plasma ions has been neglected so far, but with light ions these motions have to be considered at high magnetic fields. Fortunately, the ions can be included by a minor modification of the previous equations. Solving the equation of motion, Eq. (1) for both ions and electrons, we obtain

Eq. (34) $$\mathbf{v}_{i\perp} = \frac{i}{B_0}\frac{\delta}{1-\delta^2}(\mathbf{E} + i\delta\mathbf{E}\times\hat{\mathbf{z}}), \qquad \mathbf{v}_{e\perp} = \frac{i}{B_0}\frac{1}{1-\gamma^2}(\gamma\mathbf{E} - i\mathbf{E}\times\hat{\mathbf{z}}) \quad ,$$

where we have defined

Eq. (35) $$\delta \equiv \frac{\Omega_c}{\omega + i\nu_i}, \qquad \gamma \equiv \frac{\omega + i\nu_e}{\omega_c},$$

$\Omega_c$ being the ion cyclotron frequency. Both $\delta$ and $\gamma$ are small in the usual helicon. For simplicity, we neglect the collision frequencies $\nu_i$ and $\nu_e$ for now. Eq. (34) can be inverted to give

Eq. (36) $$\mathbf{E}_\perp = \frac{B_0}{en_0}\left[\left(\frac{1-\delta\gamma}{1+\delta\gamma}\right)\mathbf{j}\times\hat{\mathbf{z}} + i\varepsilon\mathbf{j}\right] \approx \frac{B_0}{en_0}\left[\mathbf{j}\times\hat{\mathbf{z}} + i\varepsilon\mathbf{j}\right],$$

where

Eq. (37) $$\varepsilon \equiv \frac{\delta-\gamma}{1+\delta\gamma} \approx \delta - \gamma\,,$$

the quantity $\delta\gamma$ being just the mass ratio m/M. Using Eq. (37) in place of Eq. (6), we can still keep all of our previous calculations and simply replace Eq. (27) by

Eq. (38) $$\varepsilon\beta^2 + k\beta - k\alpha = 0,$$

which reduces to Eq. (27) in the $\delta \to 0$ limit. Note that the cyclotron-resonant denominators is Eq. (34) have canceled out in Eq. (36); though the current can be infinite for given E at resonance, E is not infinite for finite current. From Eq. (37), we see that the ion mass effect is larger than the electron mass effect if $\delta > \gamma$, or $\omega < \sqrt{(\omega_c\Omega_c)}$, the lower hybrid frequency. However, even if $\varepsilon \approx \delta$, the effect of $\delta$ on the dispersion relation is not large unless the term $\delta\beta^2$ in Eq. (38) is comparable to one of the other terms, say, $k\alpha$. For $\beta \approx \alpha$, we then have $\delta = \Omega_c/\omega \geq k^2c^2\omega_c/\omega_p^2\omega$, or $k^2c^2 \leq \Omega_p^2$; that is, the wavelength must be less than the ion plasma skin depth, and this is almost never the case. The dispersion relation for argon shown in Fig. 1 actually had the ion terms included, but the effect was indiscernible. The corresponding curves for helium are shown in Fig. 7. The density is seen to increase as a result of the ion corrections, but there is no resonant behavior. One might have expected to see the lower-hybrid resonance, but that occurs only for $k_\parallel = 0$, and we have considered antennas that excite only finite-$k_\parallel$ waves. Evidence of distinct density peaks at fields close to the lower hybrid resonance has been given by Shoji

(77) in 2-mTorr helicon discharges with 1 kW of 8.5-MHz power. These peaks were seen in $H_2$, $D_2$, He, and Ne, but not in the heavier gases Ar and Xe. In a helicon-excited argon laser, Zhu and Boswell (91) saw optimal optical gain when $\omega$ was near the lower hybrid frequency. However, these effects cannot be explained by the dispersion relation alone.

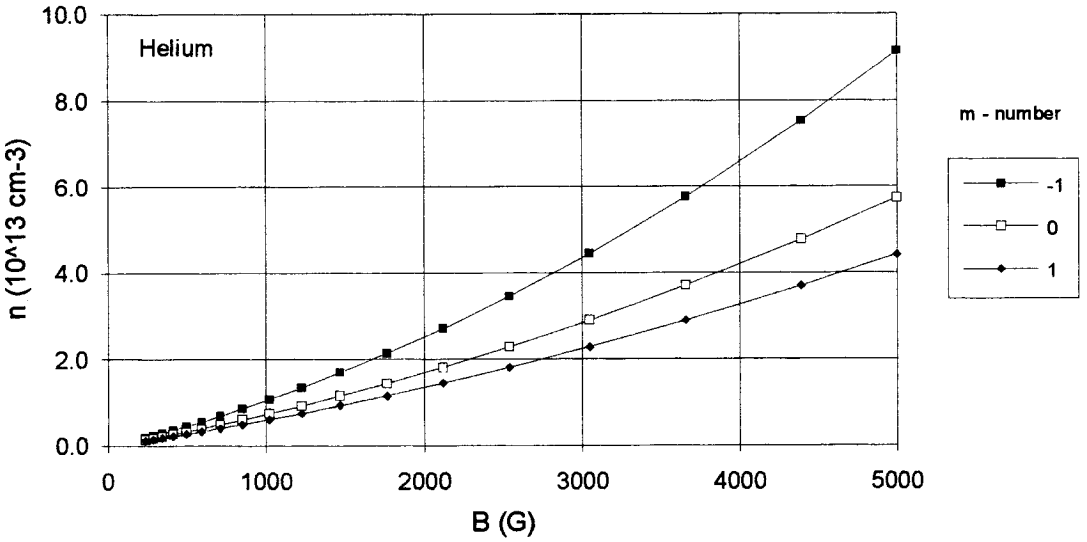


**Figure 7.** Dispersion relation for undamped helicon waves in helium. Conditions are the same as in Fig. 1.

We have made the tacit assumption that $E_z$ is zero. This cannot strictly be true if the masses are finite; but the electrons are so mobile that, in the collisionless case, very little E-field is required to drive $j_z = \mu_0^{-1}(\nabla \times \mathbf{B})_z$. Furthermore, since $E_z$ is a tangential component, it has to vanish on the boundary. Including a small but finite value of $E_z$ would cause unnecessary complications in the theory. We have also neglected dissipation up to this point. In principle, effective collision frequencies $\nu_i$ and $\nu_e$ can be included in the transverse motions by retaining these terms in Eq. (35). However, it would not be worthwhile to do this, since the main effect of collisions is in the parallel motion of the electrons. The component $E_z$ which is needed to overcome collisional drag gives rise to the absorption of the rf energy and is given by the $z$ component of Eq. (6). This is by far the dominant dissipative effect.

**Damping and energy deposition.** To treat collisional damping, let $\nu$ be the electron collision frequency against either neutrals or ions. It is related to the resistivity by Eq. (5). We now retain it in the definition of $\gamma$ [Eq. (7)], giving rise to imaginary terms

on the right-hand side of Eq. (14). If the damping is weak, the effect on the normal helicon root, $\beta_1$, would be to add an imaginary term to $\gamma$ in Eq. (15). Since $\beta_1$ satisfies real boundary conditions, it must be real, and therefore k or $\omega$ must be complex if $\gamma$ is complex. Considering spatial damping, Chen (27) finds the imaginary part of k and the collisional damping length to be:

Eq. (39)
$$\mathrm{Im}(k) \approx \frac{\nu}{\omega_c} T, \qquad L_c \approx \frac{\omega}{k} \frac{\mu_0}{\eta T^2}.$$

In this perturbation treatment, k and $T^2 = \beta^2 - k^2$ may be given their collisionless values.

In the experiments of Boswell (10), this damping rate fell short of explaining the absorption of rf energy by a factor of about $10^3$. Chen (27) has proposed that Landau damping, a collisionless mechanism in which wave energy is expended in accelerating electrons, could be responsible for the unusually efficient absorption. Fig. 8 shows a cartoon of how this occurs.

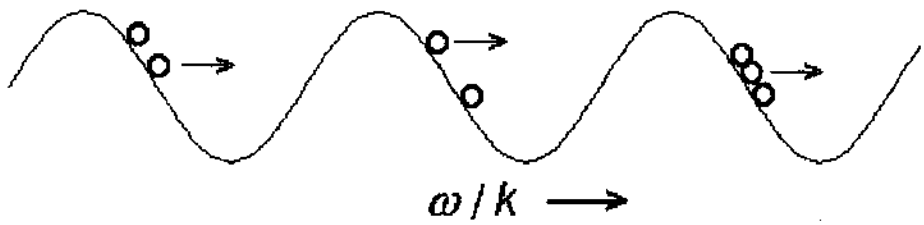


**Figure 8.** Mechanism of Landau damping. The wave represents the potential -eV, as seen by the electrons, shown as circles. Various numbers of electrons can be picked up by the wave in each wavelength.

Depending on the wave amplitude, electrons traveling near the phase velocity in their thermal motions will be caught by the wave and be accelerated by its electric field $E_z$. Only those located in the right phase of the wave will be accelerated, and the time they spend in this phase will be long if their velocities are close to $v_\phi = \omega/k$. Thus the velocity of some electrons can be increased to $v_\phi$; if it exceeds this, the electrons will soon get out of phase and be decelerated. The wave is absorbed by the loss of energy to the accelerated electrons, even in the absence of collisions. This mechanism allows the operator to adjust either $\omega$ or k so that $v_\phi$ matches the desired velocity class. We can define the "resonant energy" to be

Eq. (40) $$E_r \equiv \frac{1}{2} m v_\phi^2 .$$

If $E_r$ is near the thermal energy, many electrons will be accelerated, and the damping rate will be very large. On the other hand, these electrons are too slow to cause ionization. On the other hand, if $E_r$ is adjusted to be near the peak of the ionization cross section, say 50-150 eV, the number of resonant electrons will be small, but they will achieve the optimum energy. The Landau damping rate has been calculated by Chen (27) in terms of the plasma dispersion function $Z(\varsigma)$, which must be evaluated numerically. For $v_\phi$ several times larger than the thermal velocity, however, one can use the asymptotic expansion of $Z(\varsigma)$ and obtain the following Landau damping formulas for equivalent collision frequency and damping length:

Eq. (41) $$\nu_{LD} = 2\sqrt{\pi}\omega\varsigma^3 e^{-\varsigma^2}, \qquad L_{LD} = \omega_c / \nu_{LD} T,$$

where $\varsigma = \omega / k(2KT_e / m)^{1/2}$.

The energy deposition per unit volume is given by $W = \mathbf{j} \cdot \mathbf{E} = j_z E_z$. This is because, when the mass effects are neglected, $\mathbf{j}_\perp$ is given by the $\mathbf{E} \times \mathbf{B}$ drift and is always perpendicular to $\mathbf{E}$. Thus, $W = \eta_{eff} j_z^2$, where $\eta_{eff}$ is an effective resistivity given by inserting $\nu = \nu_e + \nu_{LD}$ into Eq. (5). Since $j_z \propto B_z$ in the lowest approximation, the energy absorption should vary radially as $B_z^2 \propto J_m^2(Tr)$. These profiles will be shown in Sec. 2.3. However, the measured density profiles do not always agree with this absorption rate.

**Antennas and polarization.** RF power is usually coupled to helicon discharges by one form or another of the so-called Nagoya Type III antenna [Okamura et al. (72), Sato et al. (76), Watari et al. (88)], shown schematically in Fig. 9. The important elements of the antenna are the two legs carrying current along the magnetic field. A rising current in the directions shown would induce an opposing electric field in the plasma which would cause space charges to build up as shown. These charges create an electrostatic field in the vertical direction which is in the same direction as that induced by the vertical currents but is larger by a factor of order $(L/a)^2$, where L/a is the aspect ratio of the antenna [Chen (22)]. Thus, the Nagoya Type III antenna not only converts the electromagnetic rf field into an electrostatic field, but also amplifies it. The horizontal

electrostatic field builds up until it just cancels the horizontal electromagnetic field because of the high mobility of electrons in that direction. In the vertical direction, however, the electrostatic field cannot be short-circuited because the electrons are restrained by the magnetic field, and that field couples strongly to the vertical electric field at the center of the mode pattern of the helicon wave (Fig. 2).

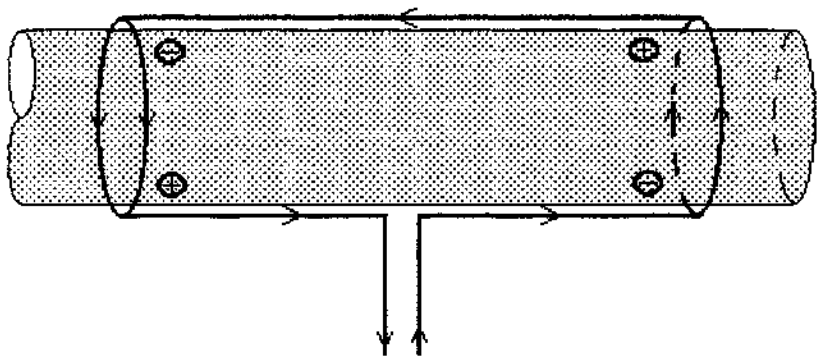

**Figure 9.** Schematic of a Nagoya Type III antenna. The arrows show the current flow direction in one phase of the rf cycle. This antenna covers a half-wavelength; longer antennas would have adjoining sections with the currents in the horizontal legs reversed.

A straight antenna such as in Fig. 9 would excite plane-polarized waves. Though purely plane-polarized helicons cannot exist, one can add an m = -1 and an m = +1 mode together with appropriately adjusted amplitudes to form a mode that is nearly plane polarized over a large region near the axis [Chen and Decker (31)].

To excite circularly polarized helicons, one can modify the Nagoya Type III antenna by making the horizontal legs helical. A "right-hand" helical antenna is shown in Fig. 10. If **k** and **B** are in the same direction--say, both to the left--then the radial electric field will rotate clockwise as the pattern propagates to the left, as is seen by an observer looking along **B**. This is an m = +1 mode. However, since the antenna field is a standing wave in the laboratory frame, it can excite waves with **k** in the opposite direction as well. Thus, if **B** is toward the left and **k** is toward the right, the E-field will rotate counterclockwise as seen along **B**, and an m = -1 wave is simultaneously excited in the opposite direction. To excite an m = -1 mode propagating to the left, one can either reverse the direction of **B**, or use an antenna wound with the opposite helicity, as shown in

Fig. 11. This is a "left-hand" antenna, which excites an m = -1 mode if **k** and **B** are parallel, and an m = +1 mode if they are antiparallel.

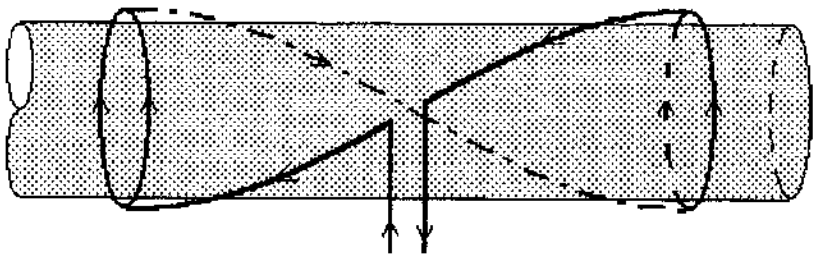

**Figure 10.** Schematic of a "right-hand" helical antenna.

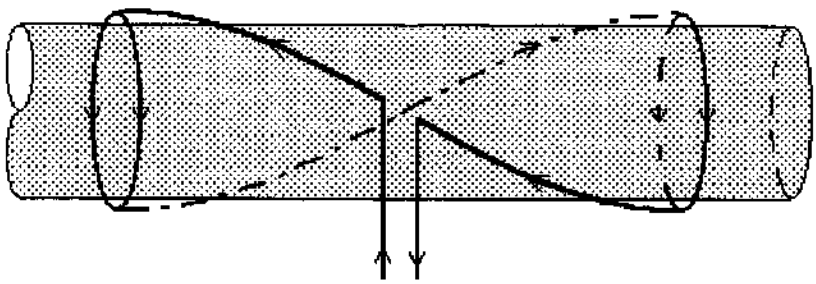

**Figure 11.** Schematic of a "left-hand" helical antenna.

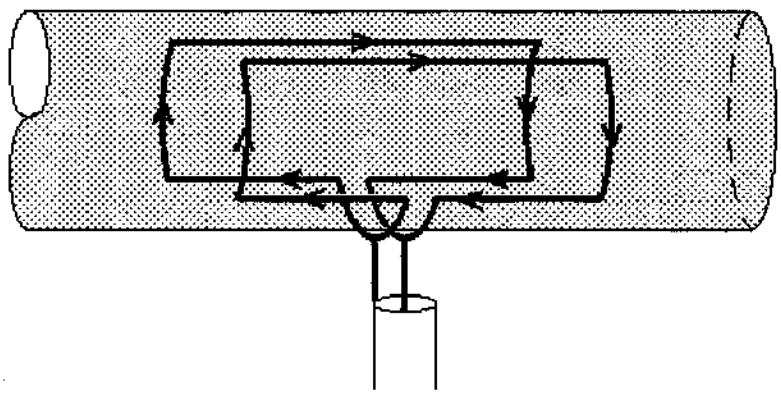

**Figure 12.** Schematic of a Boswell-type paddle-shaped antenna.

Fig. 12 shows a paddle-shaped variant of the m = 1 Nagoya Type III antenna that is preferred by Boswell and co-workers. Comparing this with Fig. 9, one sees that it is essentially the same configuration, except that the horizontal legs have been split in half and the two halves have been separated. It is claimed that the Boswell variant couples more efficiently, but measurements made by Chen and Chevalier (27) showed no difference with the standard Nagoya antenna.

It is important to note the difference between global polarization and local polarization. In Fig. 3, it is seen that, for $m \geq 1$, the entire wave pattern rotates one way or the other, depending on the sign of m/k. Thus, for $k > 0$, we refer to m = 1 as a right-hand circularly polarized mode, and m = -1 as a left-hand one. On the other hand, the local electric field can rotate in different directions at different radii, depending on the shape of the field lines as shown in Fig. 2. The local rotation direction is given by the components $B_R$ and $B_L$, as defined in Eq. (18). Since $B_R$ and $B_L$ vary with radius, as shown by Eq. (21), the local rotation of the E-field vector can change direction with radius. At the boundary, however, **E** must be plane polarized in order to be normal to the wall. At r = 0, Eq. (21) shows that $B_R$ and $B_L$ both vanish for $|m| \neq 1$; but for $|m| = 1$, those components proportional to $J_0(Tr)$ remain finite. There, the m = 1 mode has $B_R$ only, while the m = -1 mode has $B_L$ only, regardless of the sign of **k**.

### 2.3 Helicon waves in nonuniform plasmas

**Dispersion equation.** Since plasmas in practice do not maintain uniform density to the wall, we next derive the dispersion relation for helicons in an arbitrary density profile [Chen et al. (35, 86)]. If the density near the wall falls to a very low value, the displacement current is needed to sustain the wave. Hence we retain Eq. (2) but replace Eq. (3) with the full equation

Eq. (42) $$\nabla \times \mathbf{B} = \mu_0 (\mathbf{j} - i\omega\varepsilon_0 \mathbf{E}).$$

To simplify the problem, we neglect damping ($\nu = \eta = 0$), so that the curl of Eq. (6) becomes

Eq. (43) $$\nabla \times \mathbf{E} = \nabla \times \left( \frac{\mathbf{j} \times \mathbf{B}_0}{en_0} \right).$$

We now let $n_0$ be a function of $r$, so that $\alpha$, as defined by Eq. (13), is also a function of $r$:

Eq. (44) $$\alpha(r) = \frac{\omega}{k}\frac{e\mu_0}{B_0} n_0(r).$$

We next substitute Eq. (43) into Eq. (2), noting that $n_0$ is no longer constant in Eq. (43). Using Eq. (44), one obtains

Eq. (45) $$(\alpha/\mu_0)\mathbf{B} = \mathbf{j} + \frac{i}{k}\left(\nabla\cdot\mathbf{j} - \frac{\alpha'}{\alpha} j_r\right)\hat{\mathbf{z}},$$

where we have written $\alpha'/\alpha$ for $n_0'/n_0$. We see that $\mathbf{B}_\perp$ still satisfies Eq. (24), but there are two added terms in $B_z$. The small $\nabla\cdot\mathbf{j}$ term is due to the displacement current, and the $\alpha' j_r$ term gives the effect of the density gradient. The physical effect is apparent here: when there is a current along $n_0'$, a space charge builds up which must be dissipated by flowing along the magnetic field. This added contribution to $j_z$ can either add or subtract from the normal current $j_z$, depending on the sign of $m$; and this will affect the $m > 0$ and $m < 0$ modes differently.

The curl of Eq. (42) yields

Eq. (46) $$\nabla^2\mathbf{B} + \mu_0\nabla\times\mathbf{j} + k_0^2\mathbf{B} = 0,$$

where we have defined $k_0 \equiv \omega/c$. The $r$ component of this equation is

Eq. (47) $$B_r'' + \frac{1}{r}B_r' - \left(\frac{m^2+1}{r^2} + k^2 - k_0^2\right)B_r - \frac{2im}{r^2}B_\theta + \mu_0\left(\frac{im}{r}j_z - ikj_\theta\right) = 0,$$

the primes indicating $\partial/\partial r$. Here, $j_\theta$ is given in terms of $B_\theta$ by Eq. (45), and $j_z$ in terms of $B_r$ and $B_\theta$ by Eq. (42) with $E_z = 0$. With the definition

Eq. (48) $$\lambda \equiv 1 - (k_0/k)^2,$$

this yields

Eq. (49) $$B_r'' + \frac{1}{r}B_r' - \left(\frac{1}{r^2} + k^2\lambda\right)B_r + \frac{im}{r}B_\theta' - i\left(\frac{m}{r^2} + k\alpha\right)B_\theta = 0.$$

We wish to eliminate $B_\theta$ and $B_\theta'$ to get a radial equation for $B_r$. Eliminating **E** from Eq. (42) using Eq. (6) and substituting the resulting expression for **j** into Eq. (45), we can write the *r* and *6* components of Eq. (45) as

Eq. (50) $$\alpha B_r = (im/r)B_z + ik\lambda B_\theta$$

Eq. (51) $$\alpha B_\theta = ik\lambda B_r - B_z'.$$

Here, $\lambda$ is a quantity which is unity except for the displacement current correction. $B_Z$ can be eliminated from Eq. (50) by $\nabla\cdot\mathbf{B} = 0$, yielding

Eq. (52) $$B_\theta = \frac{imrB_r' + i(m + \alpha kr^2)B_r}{m^2 + \lambda k^2 r^2}.$$

To obtain $B_\theta'$, we multiply Eq. (50) by *r* and differentiate, then substitute the resulting $B_z'$ into Eq. (51). Using Eq. (52) for $B_\theta$, we obtain, after simplification, the following equation for $B_r$:

Eq. (53)

$$B_r'' + \left(1 + \frac{2m^2}{m^2 + \lambda k^2 r^2}\right)\frac{B_r'}{r} - \left[m^2 + \frac{mr\alpha}{k\lambda}\frac{\alpha'}{\alpha} - \frac{r^2}{\lambda}\left(\alpha^2 - k^2\lambda^2\right) - \frac{m^2 + kr^2(2m\alpha - k\lambda)}{m^2 + \lambda k^2 r^2}\right]\frac{B_r}{r^2} = 0.$$

This equation can be integrated numerically for arbitrary $\alpha(r)$, subject to the boundary condition $B_r = 0$ at r = a. The other components of **B** can then be obtained from Eqs. (50) and (52).

**Wave profiles.** Eq. (53) can be used to compute the wave fields for the measured density distribution. To illustrate the effect of density gradients, we have chosen a two-parameter family of curves:

Eq. (54)

$$\frac{n}{n_0} = \frac{\alpha}{\alpha_0} = \left[1 - \left(\frac{r}{a}\right)^s\right]^t .$$

These profiles are shown in Fig. 13.

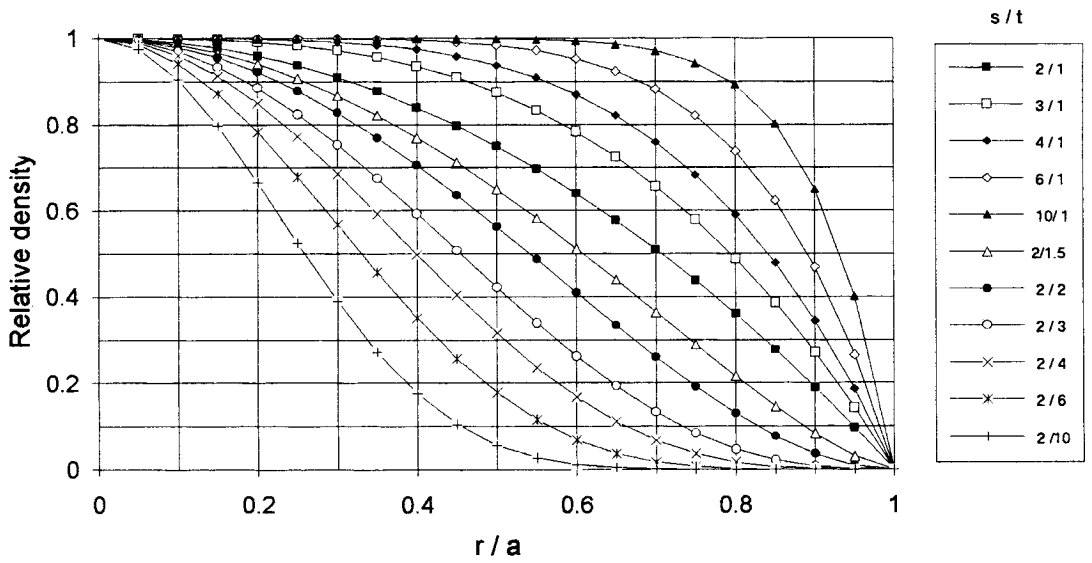


**Figure 13.** Model density profiles characterized by the parameters *s* and *t* (Ref. 35).

Fig. (14) shows the wave profiles for the three principal azimuthal modes for uniform (t = 0) and parabolic (s = 2, t = 1) density profiles. The field patterns for the m = 1 and -1 modes in a parabolic profile are shown in Fig. 15. As expected, the patterns are narrower than for the uniform case in Fig. 2. Moreover, it is apparent that the m = -1 mode is considerably narrower than the m = +1 mode. The change in the $B_z$ profile with density profile, as given by the parameters *s* and *t*, is shown in Fig. 16 for these two modes. For each case, the m = 1 mode is broader than the m = -1 mode.

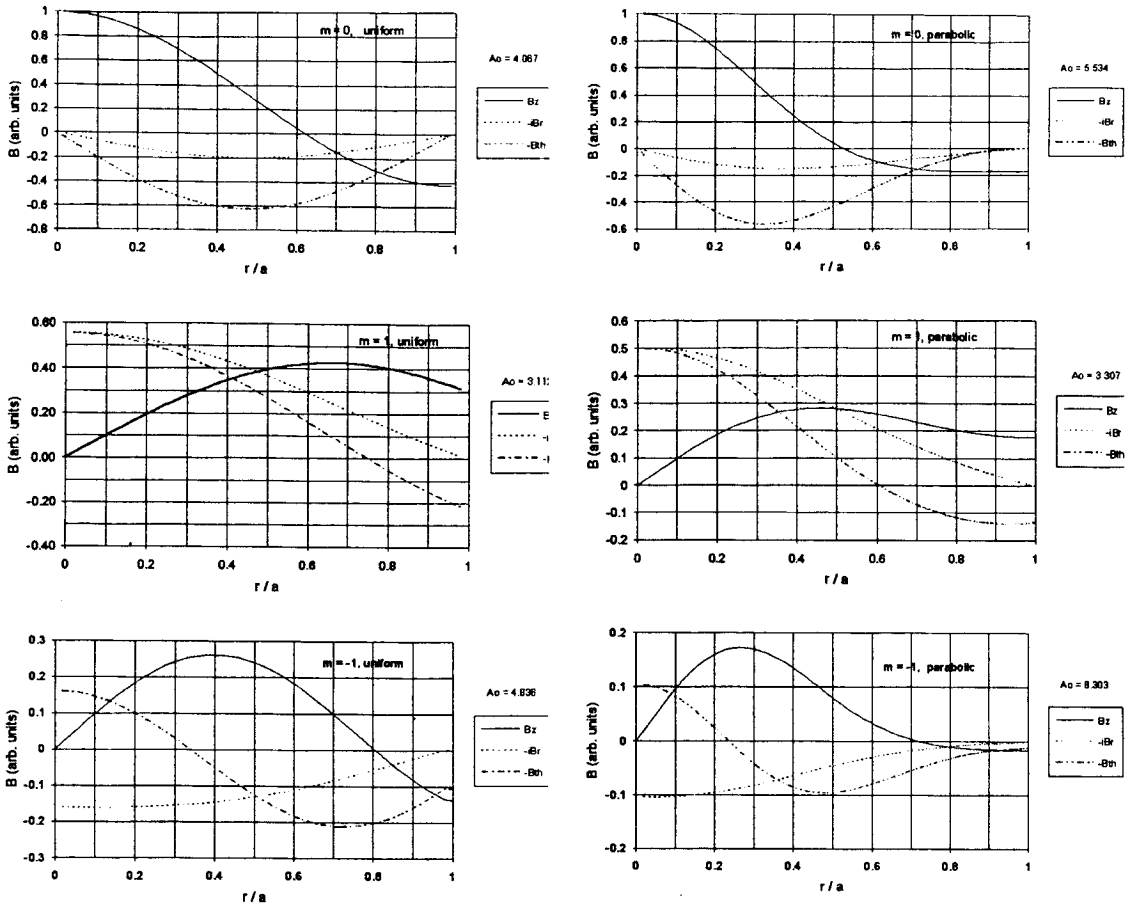


**Figure 14.** Computed profiles for $B_Z$, $B_r$, and $B_\theta$ for the m = 0, +1, and -1 modes in uniform and parabolic density distributions. The parameters were f = 27.12 MHz, a = 5 cm, and $\lambda$ = 24 cm. The eigenvalue $\alpha_0 = \alpha(0)$ for each case is labeled as Ao and is related to the density on axis by Eq. (44) (Ref. 35).

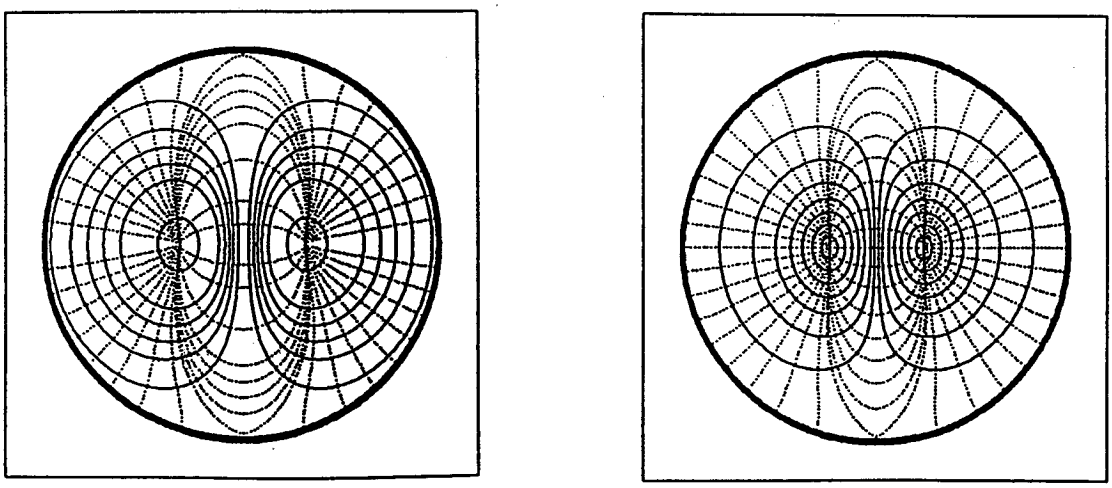

m = +1

m = -1

**Figure 15.** Pattern of magnetic (solid) and electric (dashed) field lines in the m = +1 and -1 modes of the helicon wave in a parabolic density profile (Ref. 35).

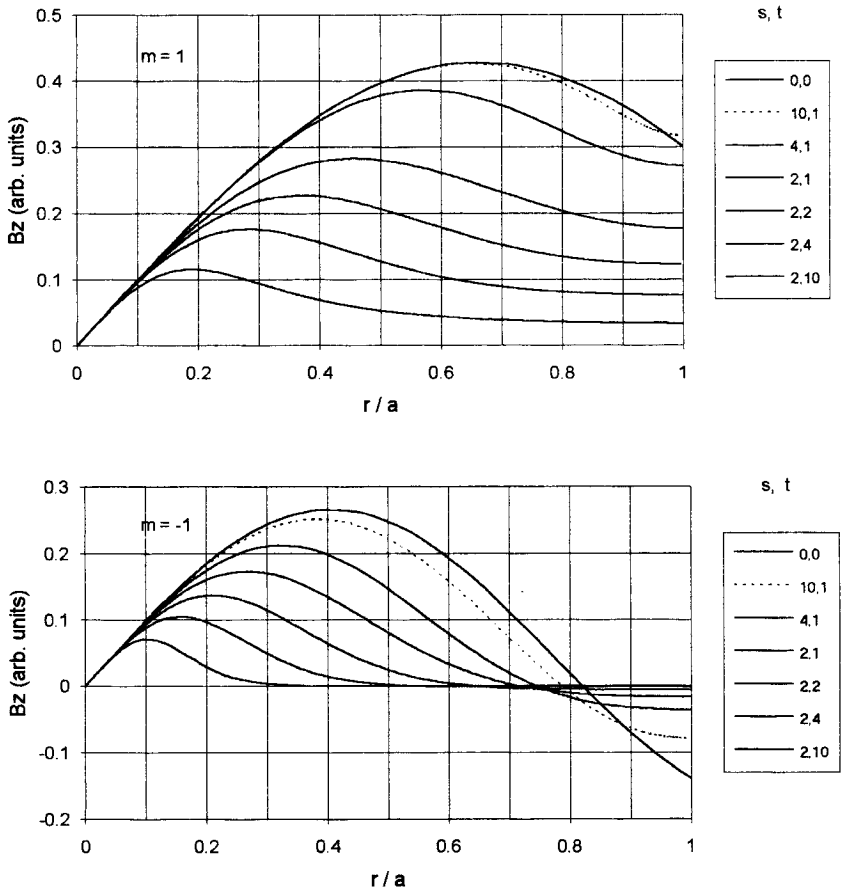


**Figure 16.** Change of the $B_Z$ profile with the density profile parameters *s* and *t* for the m = +1 (top) and m = -1 (bottom) modes (Ref. 35). Other values are as in Fig. 14.

As the density profile sharpens, the peak density, as given by $\alpha(0) \equiv \alpha_0$ for fixed $B_0$, increases; but the increase is much larger for m = -1 than for m = 1, as shown in Fig. 17. For the m = 1 mode, the density on axis increases only slightly as the density profile is changed from t = 0 to t = 10, for s = 2. However, for the m = -1 mode, the resonant density increases by an order of magnitude. These results indicate that very dense, narrow columns can be produced with the m = -1 mode, while broad, uniform plasmas would be better created by the m = 1 mode. A difference in the visual appearance of helicon discharges upon reversal of the dc magnetic field or the helicity of the antenna had been reported by both Shoji and Chen in 1992 (unpublished). The change from wide to narrow plasmas seems to be related to the heretofore unrecognized difference between the m =1 and -1 modes. However, this is not the entire story, because Light and Chen (66)

have observed that the m = 1 mode is preferentially excited in all cases (cf. Sec. 3.2), possibly because the energy absorption is higher for the m = 1 mode as a result of the $\alpha'$ term in Eq. (45) [Chen et al. (35)].

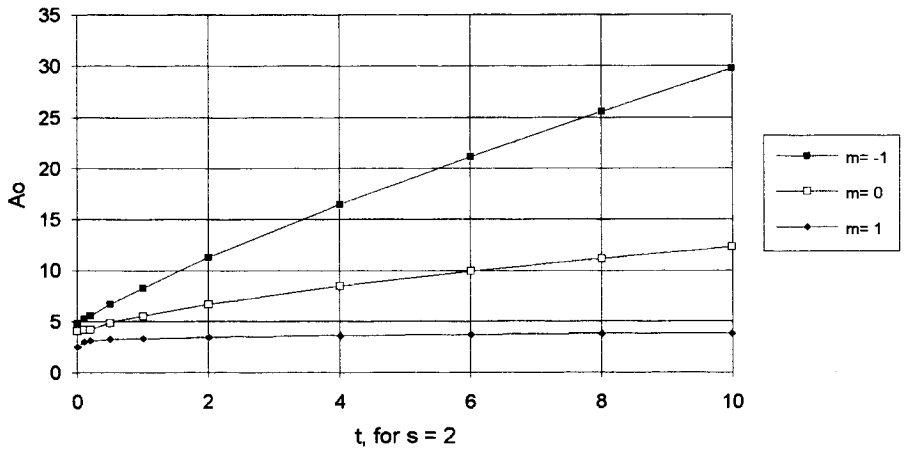


**Figure 17.** Increase in central density, proportional to Ao = $\alpha_0$, with sharpness parameter *t* (Ref. 35).

**Self-focusing of helicon discharges.** Since the energy deposition, and hence the ionization rate, is roughly proportional to $B_z^2$, the profiles of Fig. 16 show that a positive feedback mechanism will cause the density profile to become progressively narrower until diffusion stops the process. This self-channeling or self-focusing effect should be stronger for the m = -1 mode than for the m = 1 mode. However, this effect has not been experimentally confirmed. In fact, the m = 0 mode, which has its energy absorption peak on axis, should give the narrowest plasmas of all; but in practice, the opposite is observed. Campbell et al. (19) have shown that the m = 0 mode creates more uniform plasmas than the m = 1 mode, possibly because of surface absorption processes.

## 3.0 EXPERIMENTAL TESTS OF THEORY

It is difficult to compare results from different laboratories because the results are often device-dependent. Furthermore, the most common diagnostic, the Langmuir probe, is subject to errors caused by rf pickup; and the degree of cancellation of these rf signals differs among experimenters. Even the measurement of pressure varies widely, not only because of the placement of the pressure gauge relative to the pump and the gas inlet, but also because of pulsed operation. The most detailed measurements are made with pulsed plasmas because probes cannot survive in the very high densities of helicon discharges. In that case, not only does the neutral pressure inside the plasma differ from that outside, but even the ambient pressure changes during the pulse, depending on the fraction of the vacuum chamber that the plasma occupies. In the absence of a "reference cell" for helicon sources, comparisons between laboratories are dangerous; but, nonetheless, considerable progress has been made.

Devices used to generate helicon waves fall into three main classes. The first, which we shall call Type A (Fig. 18), consists of a glass or quartz tube about 5 to 10 cm in diameter and 1 to 2 meters long. It is immersed in a uniform magnetic field of up to 3 kG, but more typically, 1 kG. The rf antenna covers a small part of the length and may be located at one end or in the middle. The second, Type B (Fig. 19), consists of a large chamber 0.5-1 m in diameter by 1 to 2 meters long, to one end of which a source is attached to inject the plasma. The source is typically 10-20 cm in diameter and 20-50 cm long, around which the antenna is wound. The magnetic field coils around the source are usually smaller than those around the main chamber, and there may be a change in the field strength between the two regions. Type C sources (Fig. 20) are intended for etching applications, and the magnetic field is vertical so as to direct the plasma toward a horizontally mounted wafer. The source is typically 10 cm in diameter and as short as possible to keep the unit compact. For economy, the magnet coils are few in number, and the magnetic field is therefore not uniform. The plasma streams from the source into a field-free region in which there may or may not be surface fields provided by permanent magnets (a "magnetic bucket"). Type A devices most closely resemble the conditions assumed in the theory and are best suited for establishing the validity of theoretical predictions. Their small diameters, however, make probing difficult; and the small volume of gas surrounding the plasma is not a sufficient plenum to maintain the neutral pressure during each discharge pulse. The large experimental chamber in Type B devices avoids this difficulty, but the boundary conditions acting on the helicon waves are no longer

uniform. In Type C devices, the magnetic field is so nonuniform that it is often difficult to ascertain that a helicon wave is excited at all. Because it produces the highest densities, argon gas is universally used in helicon studies except those in which actual etching is done.

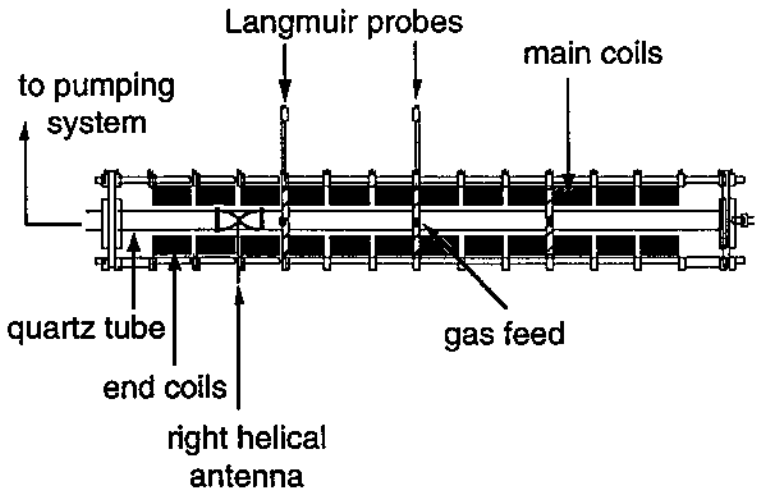


**Figure 18.** Typical Type A helicon discharge configuration (Ref. 85).

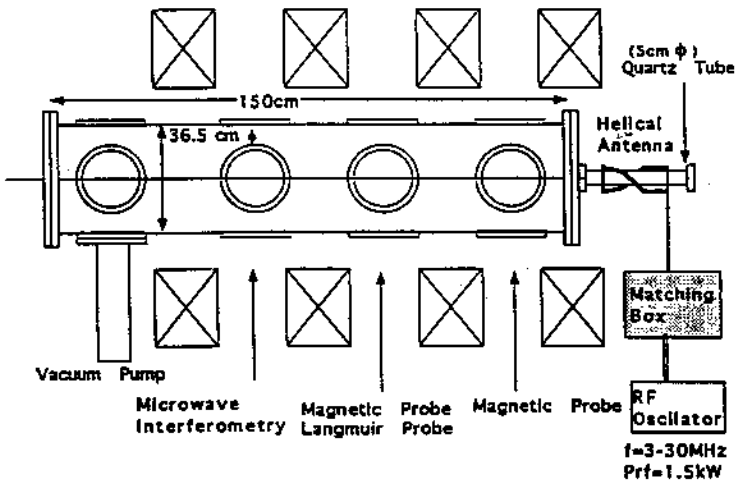


**Figure 19.** Typical Type B helicon discharge configuration (Ref. 82).

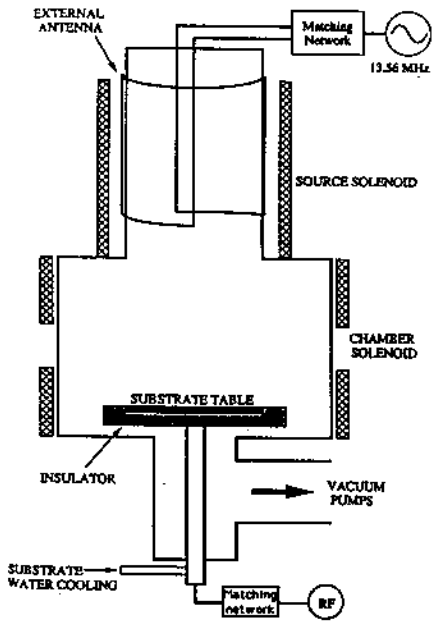


**Figure 20.** Typical Type C helicon discharge configuration (Ref. 74).

### 3.1 Dispersion relation

The dispersion relation for classical helicon waves is given by Eq. (13), with $\alpha = \beta$ and $\beta$ given by Eqs. (7) and (26). Thus, $\alpha$ is a number related to the tube radius $a$. In the lowest approximation, we can estimate $\alpha$ in long, thin tubes by assuming $k << T \approx \beta \approx \alpha$, so that the second term in Eq. (26) can be neglected, and we have $J_m(Ta) \approx J_m(\alpha a) \approx 0$. Since the first root of $J_m(z)$ is 3.83, Eq.(13) can be written

Eq. (55) $$\frac{\omega}{k}\frac{n_0}{B_0} = \frac{1.9\times 10^{25}}{a} \quad \text{or} \quad \frac{n_{13}}{B_G} = \frac{1.9}{a_{cm}\lambda_{cm}f_6},$$

where $n_{13}$ is the density in units of $10^{13}$ cm$^{-3}$, $B_G$ is in gauss, $f_6$ is frequency in MHz, and $a_{cm}$ and $\lambda_{cm}$ are in cm. In terms of the resonant energy $E_r = m(\omega/k)^2/2$, Eq. (55) can be written

Eq. (56) $$\frac{n_{13}}{B_G} = 0.032/a_{cm}\sqrt{E_r(eV)}.$$

If the value of k follows that set by the antenna length, then once the frequency and tube diameter are set, the ratio $n_0/B_0$ should be a constant, whose value is approximately given by Eq. (55).

The linear relationship between *n* and *B* was first seen by Boswell (10) in a Type A device, as shown in Fig. 21. The variation was not smooth, however, with jumps attributed to standing wave resonances. Later, in a Type B device called WOMBAT, Boswell and Porteous (12) found a smooth *n-B* curve, but there were jumps in density as the rf power, $P_{rf}$, was increased. This effect was also seen by Boswell et al. (11, 13) in a

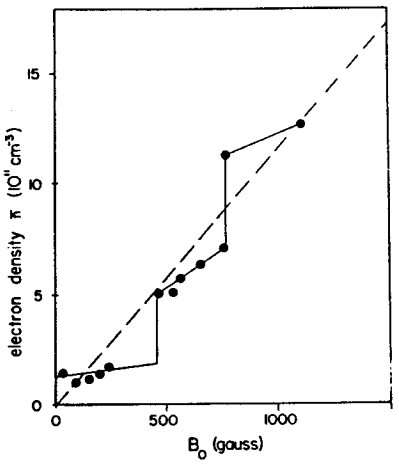


**Figure 21.** Stepwise linear *n-B* relation observed at low power (180 W) and 1 kG (Ref. 10).

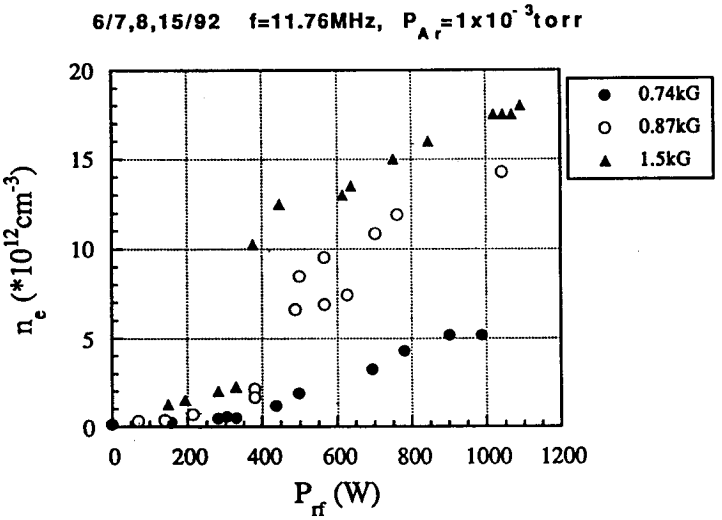


**Figure 22.** Discontinuous jump in density with increase in rf power (Ref. 82).

Type A machine, by Perry et al. (74) in a Type C device, and by Shoji (77, 82) in a Type B machine, as shown in Fig. 22. Jumps in n-$P_{rf}$ curves in a Type C device were also seen by Nakano et al. (71) in a $Cl_2$ plasma and were attributed to standing wave resonances. Using a Type A device, Chen et al. (34) later found that these observations were manifestations of a threshold effect in both B and $P_{rf}$, as shown in Figs. 23 and 24. The linear n-B dependence is not established unless the magnetic field is above 400-500 G and the rf power above 400-500 W. These thresholds are somewhat lower with Nagoya Type III antennas [Chen and Chevalier (34)]. Below the threshold, a helicon wave satisfying Eq. (55) cannot be excited, but there is nonetheless non-resonant ionization by the rf field. The density jump between resonant and non-resonant discharges is demonstrated dramatically by relaxation oscillations observed near the threshold [Chen (25)]. The slope

of the n-B curves can be used in Eq. (56) to deduce the value of $E_r$, the energy of electrons traveling at the wave velocity. This quantity is plotted against $B$ in Fig. 25. It is seen that, when $B$ is well above the threshold value of ≈500G, $E_r$ converges to the range between 50 and 150 eV, just at the peak of the argon ionization cross section. Thus, not only is the linear n-B relationship established, but the coefficient in Eq. (55) or (56) has a value which one might expect for the production of primary electrons of the optimal energy.

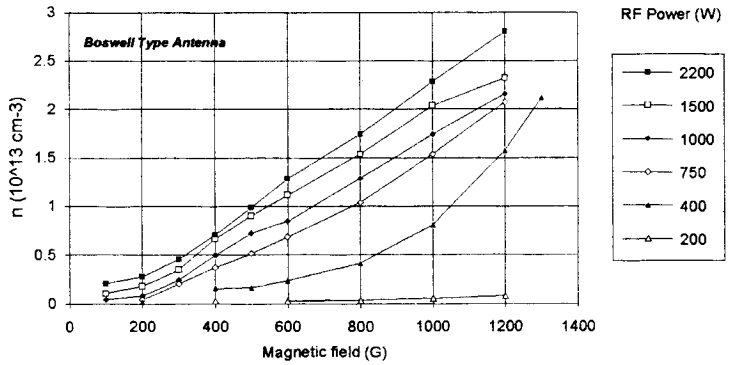


**Figure 23.** Density vs. magnetic field in a Type A device with 2 kW applied to a Boswell-type antenna (Ref. 34).

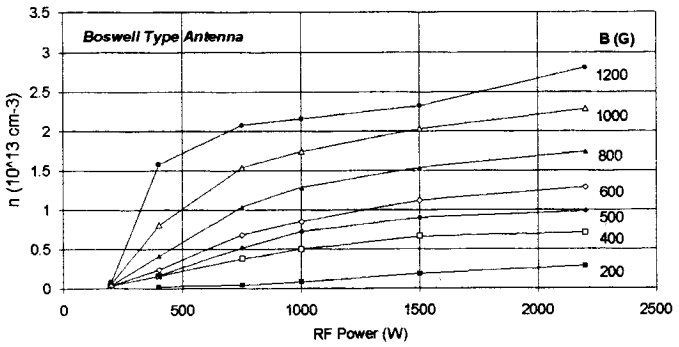


**Figure 24.** Density vs. rf power in a Type A device with B ≈ 1 kG (Ref. 34).

Direct measurements of the axial wavenumber k are difficult in Type A devices, since an internal probe shaft movable in the axial direction tends to interfere with the discharge. However, measurements are possible with external detectors or with axial probes in Type B or Type C devices. Komori et al. (61), in a Type B device, used a

reasons can be found for the predominance of m = +1 in this experiment, but the correct explanation is not yet known.

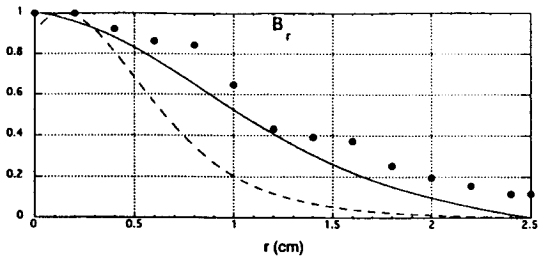


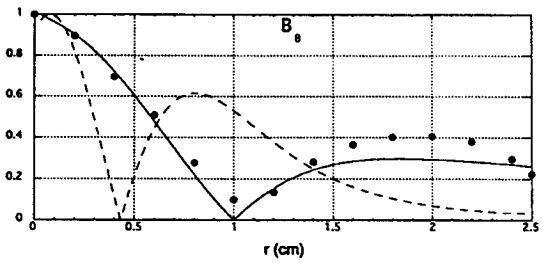


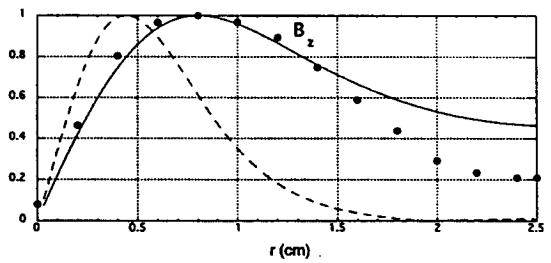


Fig. 28

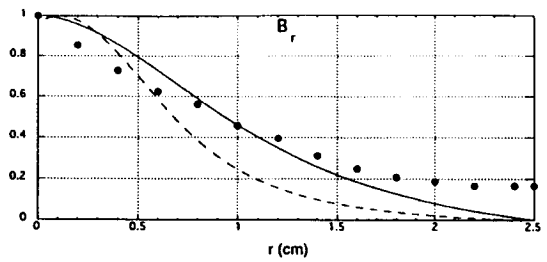


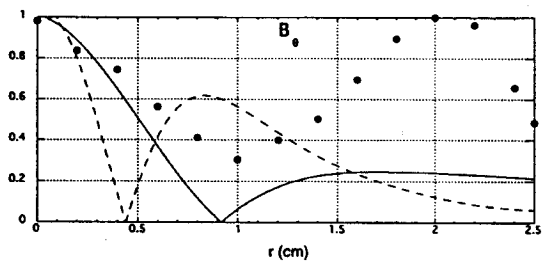


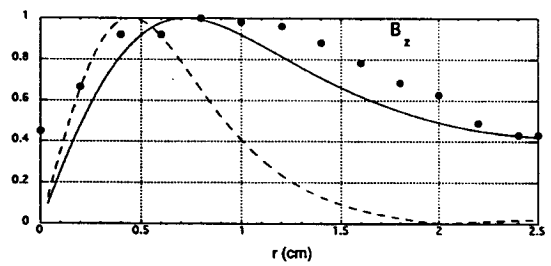


Fig. 29

**Figure 28.** Measurements of the normalized magnitudes of $B_r$, $B_\theta$, and $B_Z$ for R-wave excitation (Fig. 10) in a 5-cm diam discharge at 800 G with 1.9 kW of rf at 27.12 MHz (Ref. 66). The theoretical curves for the m = +1 (solid) and m = -1 (dashed) modes were computed from the measured density profiles.

**Figure 29.** Same as Fig. 28 but for L-wave excitation (Fig. 11).

### 3.3. Landau damping

The hypothesis that Landau damping occurs in the absorption of rf energy by helicon waves is supported by evidence of fast electrons traveling at the phase velocity of the wave. The first such evidence was provided by Zhu and Boswell (91), who made an argon laser using a Type A helicon device with high density and magnetic field. The

the order of the thermal electron energy, not that of the primary electrons. It is not yet clear which is the best resonant energy on which to base the design.

It is also possible to make axial phase measurements spectroscopically. Using a photodetector, Ellingboe et al. (46) found that Ar II radiation has a remarkably large modulation at the rf frequency. Using a movable detector in a Type B device, they determined that, in this case, the wavelength of the waves was the same as that set by the antenna.

### 3.2 Wave patterns

The first measurements of the wave magnetic field components were made by Boswell (10) in a Type A device with a dc field of 33 G and 180 W of rf power at 8.6 MHz, producing densities of order $10^{11}$ $cm^{-3}$. Using a 50-turn coil as a magnetic probe, he detected standing waves in the axial direction, with a wavelength that was not constant. He also measured the radial profiles, but they could not be fit to theory unless the collision frequency was increased to 1000 times its normal value. We now know, however, that the low field and rf power used were below threshold, and what was measured was probably not the classical helicon. At these low fields, the finite Larmor radius of the primary electrons has to be taken into account. Eight years later, Shoji (82) measured the B-components and the phases between them in the m = 0, 1, and -1 modes in a Type B device with $B_0$ = 750 G, $P_{rf}$ = 1.1 kW at 8.9 MHz, p = 1.4 mTorr of argon, and densities of order $10^{13}$ $cm^{-3}$. The radial profiles were in reasonable agreement with theory. The axial variation of phase was also measured and there was again evidence that k varied as the wave left the antenna.

Extensive data on radial profiles of helicon wave fields in a Type A device have recently been given by Light and Chen (66), who used the magnetic probe design of Shoji, consisting of a single loop at the end of a thin, rigid coaxial cable. Fig. 28 shows the fields excited by a right-hand helical antenna, compared with theoretical curves for m = $\pm$1 computed from Eq. (53) using the measured density profile. Similar data for a left-hand antenna are shown in Fig. 29. It is seen that the m = 1 case agrees well, but the left-hand antenna does not excite an m = -1 mode. In particular, the zero of $B_\theta$, where the phase is observed to jump by 180°, occurs at the radius predicted for m = +1 in both cases. The Nagoya Type III antenna also was found to excite an m = 1 mode pattern. Several

reasons can be found for the predominance of m = +1 in this experiment, but the correct explanation is not yet known.

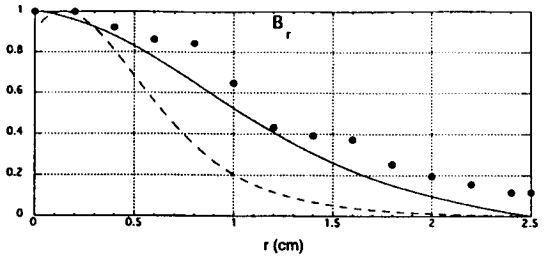


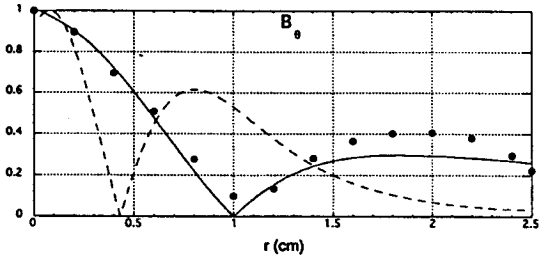


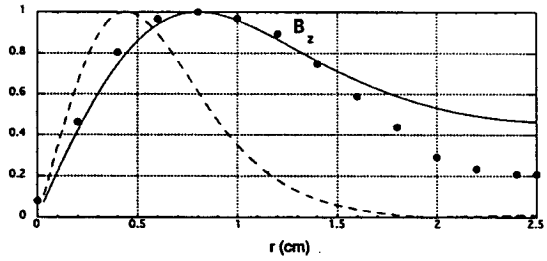


Fig. 28

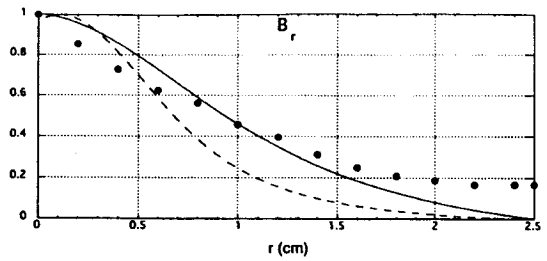


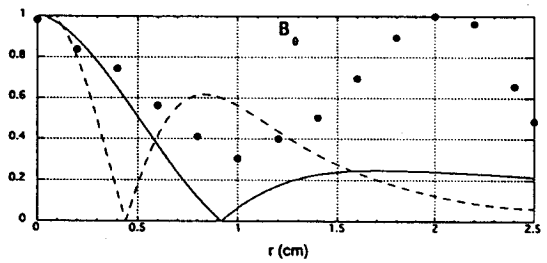


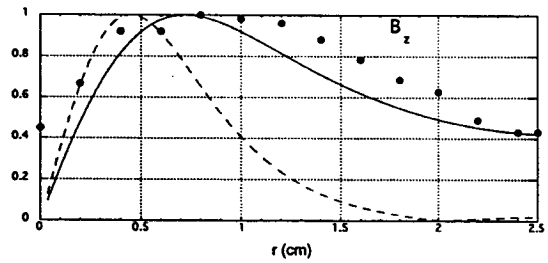


Fig. 29

**Figure 28.** Measurements of the normalized magnitudes of $B_r$, $B_\theta$, and $B_z$ for R-wave excitation (Fig. 10) in a 5-cm diam discharge at 800 G with 1.9 kW of rf at 27.12 MHz (Ref. 66). The theoretical curves for the m = +1 (solid) and m = -1 (dashed) modes were computed from the measured density profiles.

**Figure 29.** Same as Fig. 28 but for L-wave excitation (Fig. 11).

### 3.3. Landau damping

The hypothesis that Landau damping occurs in the absorption of rf energy by helicon waves is supported by evidence of fast electrons traveling at the phase velocity of the wave. The first such evidence was provided by Zhu and Boswell (91), who made an argon laser using a Type A helicon device with high density and magnetic field. The

intensity ratio of $Ar^{++}$ to $Ar^{+}$ lines indicated a population of fast electrons in the 15-50 eV range, in agreement with the range of $E_r$ deduced from measured wavelengths. More indirect evidence of electron acceleration came from the Type A experiment of Chen and Decker (32). Fig. 30 shows the floating potential of an endplate inserted at the end of the discharge away from the antenna. Though the electron temperature was only 3-4 eV, the endplate charged to more than 200 V negative relative to a grounded ring at the midplane, indicating the presence of an energetic electron tail. The endplate potential was more negative as the magnetic field, and, hence, the density and collisionality, decreased, until, at about 40 G, the potential took a reproducible jump upwards. The field at which this occurred agreed with that at which fast electrons in the 50 eV range would have large enough Larmor radii to hit the wall. Apparently, electrons accelerated by the Landau mechanism are rapidly thermalized by elastic collisions, and a fraction of these electrons are lost when the magnetic field falls below a critical value. Moreover, the endplate potential was found to decrease with the distance away from the antenna; that is, with the distance available for acceleration.

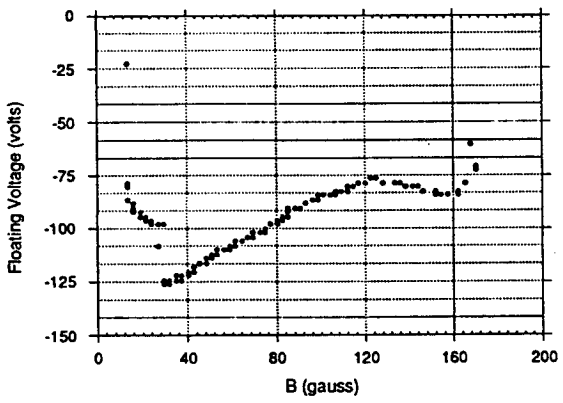


**Figure 30.** Floating potential of an endplate vs. magnetic field (Ref. 32).

Direct measurements of the fast electron tail are difficult to make reliably because of the problem of nonlinear distortion in the *I-V* curves of probes and velocity analyzers caused by rf pickup. The first attempt was made by Zhu and Boswell (92) in their Type A machine, named BASIL, under intense conditions (750 G, 3.5 kW at 7 MHz, $10^{14}$ $cm^{-3}$ density). When the rf power exceeded 2 kW, the Langmuir probe trace showed a distinct bump at small negative voltages, suggestive of a high-energy population. The electron distribution function f(v) was not calculated from the measured I-V curves, however; rather, model distributions were used to reproduce the measured curves by calculation.

The results suggested the existence of a maximum in f(v) at 30-80 eV and a minimum at 20-30 eV. These are reasonable values, but there were disquieting features. Because of the high powers used, the discharge was necessarily pulsed. The energy and magnitude of the fast electron tail were found to change on a time scale of 1 ms, which is much longer than the confinement time of the electrons. Furthermore, the rf compensation scheme was not described. Similar results were obtained by Loewenhardt et al. (68) in an entirely different machine, a toroidal heliac fusion experiment with a complicated magnetic geometry. Nonetheless, the electron f(v) was measured by probes, as shown in Fig. 31. It was seen that an electron tail developed when the magnetic field exceeded about 1 kG. Recently, Ellingboe et al. (46) have detected the phase of optical emission from $Ar^+$ lines relative to the rf cycle at variable distances from the antenna in a Type B device. The amount of modulation suggests an appreciable population of electrons of more than 20 eV energy, and the phase yields the wavelength and phase velocity, which agrees with these energies.

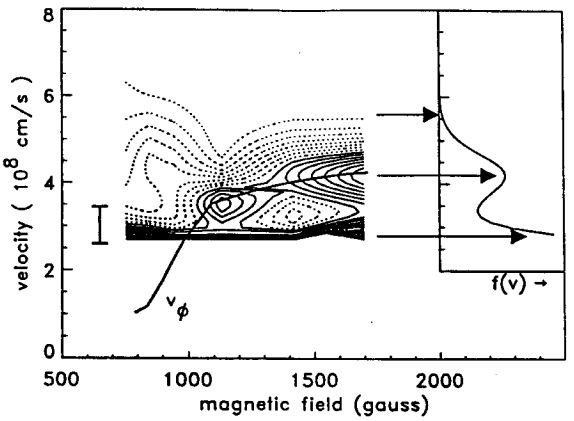


**Figure 31.** Contour plots of the electron distribution function f(v) in a fusion experiment using helicon waves for plasma creation (Ref. 68).

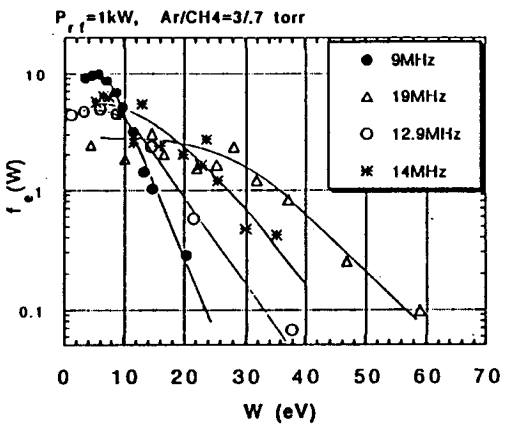


**Figure 32.** Electron energy distribution f(W) in an $Ar/CH_4$ helicon discharge at various rf frequencies (Ref. 80).

Control of the electron f(v) by varying the phase velocity $\omega/k$ has been demonstrated by Shoji et al. (80) in an argon/$CH_4$ plasma. Fig. 32 shows the energy distribution measured by a velocity analyzer as a function of rf frequency for constant antenna length. The broadening of the spectrum to higher energies as $\omega$ is increased can be seen. Finally, in the aforementioned experiment of Komori et al. (61), the damping rate Im(k)/Re(k) was also measured and compared with the Landau damping length given by Eq.(41). If no other damping mechanism existed this would imply that the maximum

density occurred when $\zeta$ was of order $\sqrt{2}$, or with $E_r$ in the range of the thermal electron energy. This result differs from that by Chen and Chevalier (34), who found that the optimum density required $E_r$ to be the energy of the ionizing electrons. The question of which is the optimum $E_r$ is still undecided.

## 4.0 DESIGN OF HELICON SOURCES

### 4.1 Basic parameters

Though it is possible to operate a discharge with a helicon antenna under non-resonant conditions, the highest efficiency is obtained when the density and magnetic field obey the helicon dispersion relation, Eq. (56). This relation is an approximate one which may be adequate for design purposes. A more accurate formula can be obtained by assuming a density profile and using the computed dimensionless value of $\alpha_0$ given in Fig. 17. In that case, Eq. (56) should be replaced by the formula [Chen et al. (35)],

Eq. (57)
$$\frac{n_{13}}{B_3} = 8.38\left(\frac{\alpha_0}{a_{cm}}\right)E_r^{-1/2}(eV),$$

where $B_3$ is the magnetic field in kG. At pressures below a few mTorr, it is likely that Landau damping will be the dominant absorption mechanism. In that case, the frequency and antenna length are determined by setting $E_r$ to match either the thermal energy or the energy of primary electrons. Eq. (57) then gives the magnetic field necessary to achieve any density in a tube of given size. In choosing the radius $a$, an important consideration is the aspect ratio of the antenna, which, for good coupling, must be neither too slender nor too squat. A value of 0.5 to 1 for $ka$ is reasonable. This and the $E_r$ condition then fix $\lambda$ and $a$ if $f$ is 13.56 MHz. A multiple or submultiple of this frequency may be desired if $a$ is unusually small or large. At high pressures and densities where collisional damping dominates, there is no longer a constraint on $\omega/k$. In that case, Eq. (57) can be written

Eq. (58)
$$\frac{n_{13}}{B_3} = 79\,\alpha_0\frac{ka}{f_{MHz}\,a_{cm}^2}.$$

Here $ka$ is the antenna aspect ratio, $\alpha_0$ is $\approx$3.83 for uniform plasmas and higher for peaked profiles. Because of the problems of gas feed discussed below, the choice of tube radius $a$

is the critical one here which determines the general behavior of the discharge. The operating frequency is not critical, but 13.56 MHz works well for tubes of 10-20 cm diameter, while 6.78 MHz is more suitable for larger tubes and 27.12 MHz for smaller tubes.

### 4.2 Discharge physics

The mechanisms of plasma creation and loss in helicon discharges are not sufficiently well known, even in the case of uniform magnetic fields, for attempts at predicting the observed profiles to be successful. In particular, the axial fall-off of plasma density with distance from the antenna seems to be sensitive to such factors as neutral pressure, antenna design, antenna tuning, grounded electrodes and probes exposed to the plasma, magnetic field uniformity, etc. In small diameter tubes, in particular, the axial density scale length may be much shorter than calculated damping distances and may be related to depletion of neutrals or formation of double layers. Discharges have even been observed to propagate into a magnetic field-free region and around a U-bend in the tube [Chen and Chevalier, 34)]. We do not know whether the ionizing energy is carried away from the antenna by the helicon waves or only by accelerated primary electrons. What follows, therefore, is not a description of the discharge equilibrium but only an account of the problem areas that require study as a prelude to meaningful computer simulations.

**Ionization processes.** In normal gas discharges with internal electrodes, ionization of neutral atoms is caused by "primary" electrons accelerated by the electric field in the cathode sheath to tens of eV (hot cathodes) or hundreds of eV (cold cathodes), sufficient to ionize an atom in a single collision. However, these primaries make many inelastic collisions, on the average, for each ionizing collision. so that the average energy required to made an ion-electron pair is of the order of 200 eV, even though the threshold ionization energy $E_i$ for argon, say, is only 15.8 eV. A purely Maxwellian electron distribution at a typical temperature of a few eV, or a slightly asymmetrical distribution carrying a current, can ionize only through the small number of electrons with energies above $E_i$ in the tail of the distribution. At low values of $E/p$, this process is aided by the formation of metastable atoms, which, instead of immediately radiating away their energy of excitation, have a finite probability of transferring it to another atom, which it ionizes. This mechanism, known as the Penning effect [Druyvesteyn and Penning (45)] was observed long ago in neon discharges with a small percentage of argon, in which an argon atom can be ionized by colliding with a neon atom in a 16.6-eV metastable state. This can

also happen in pure argon plasmas because the resonant state--that is, the lowest radiating excited state--can be mixed with the metastable states and have a lifetime of the order of a microsecond. The mean free path of the resonant photons can be very short, so that they diffuse by traveling from one atom to another in successive excitations and de-excitations. Thus, the propagation of ionizing energy can be dominated by photon transport rather than by the diffusion of primary electrons [Wamsley et al. (87), Lawler et al. (63)]. Though multi-step ionization occurs in very weakly ionized plasmas such as the positive columns, discharges at low pressures have $E/p$ values large enough to cause ionization in a single collision. Nonetheless, direct measurements of the metastable $Ar^+$ density in a helicon discharge by Giapis et al. (50) showed that metastables accounted for as much as 24% of the ion density.

The key to a high degree of ionization is efficient production and preservation of primaries. At low pressures, primaries are lost to the walls before they have deposited most of their energy in the plasma. Although the sheaths on the walls reflect electrons, the most energetic primaries are not contained. To conserve the energy expended in creating the primaries, magnetic fields can be used to restrict the losses in the directions perpendicular to the field. The PIG ( Phillips Ionization Gauge) discharge, or reflex arc, and the ECR discharge operate on this principle. In the present context, magnetic "buckets", or surface magnetic fields created by permanent magnets [Limpaecher and MacKenzie (67) are often used. These surface fields reflect the primary electrons and permit more efficient utilization of their energy.

In electrodeless discharges, the primary electrons gain energy inside the main plasma volume rather than in a cathode sheath. In ECR discharges, this would be at the resonance layer, where the magnetic field is around 875 G, at which the electron cyclotron frequency resonates with the microwave frequency of 2.45 GHz. The electrons gain energy in the directions perpendicular to the magnetic field; but, as in all discharges mentioned here, elastic scattering of electrons is so rapid that the velocity distribution of primaries quickly becomes isotropic. In RFI discharges, the primaries are created in a layer near the antenna, where the rf field is strongest. In helicon discharges, primaries can be created throughout the plasma volume, wherever the rf field is strong. Non-resonant ionization can occur, especially in the near-field of the antenna, when the helicon dispersion relation is not satisfied and the rf energy is randomly dispersed. When there is a true helicon wave, electrons are accelerated by the induced electric field which is necessary to drive the current $j_z$ along $\mathbf{B_0}$. The $\mathbf{E} \times \mathbf{B}$ velocities are necessarily smaller

than thermal velocities, and therefore there are no primaries accelerated perpendicular to **B**. At high densities, collisions with ions or neutrals scatter the electrons, and they gain energy more or less randomly. At low densities, some electrons can be trapped in the wave and be accelerated up to the phase velocity, remaining in synchronism with the wave. This is the phenomenon of Landau damping. After losing a large fraction of its energy in an inelastic or ionizing collision, a primary electron can be reaccelerated before it is lost or returned to the thermal distribution. Therefore, the production of primaries is intrinsically more efficient than in a cathode sheath. The magnetic field confines the primaries in the radial direction, and the sheath at the ends of the field lines provided partial confinement in the axial direction. After leaving the source region, primaries can be confined by multicusp surface fields, as mentioned above. The cross-over density at which collisional damping and Landau damping , as given by Eqs. (39) and (41), are equal is typically between $10^{13}$ and $10^{14}$ $cm^{-3}$. Both processes, therefore, could be operative at different radii in the same discharge, with collisional damping dominant near the axis and Landau damping dominant in the low-density region near the wall. In that case, one might expect the acceleration of primaries to take place near the periphery of the discharge rather than at the center.

**Transport processes.** Since helicon sources must have an imbedded magnetic field, transport processes in them are more complicated than in unmagnetized RIE and RFI discharges. There are at least four species of particles to consider. Thermal electrons, primary electrons, ions, and neutrals. Neutrals are not affected by electric and magnetic fields and will move at their thermal speed. Thermal electrons at 3-5 eV will have small Larmor radii and be confined in the direction perpendicular to $\mathbf{B_0}$. These electrons will diffuse across the field by colliding with either ions or neutrals. If the fractional ionization is above a few percent, collisions with ions will dominate. However, the usual formulas for diffusion in a fully ionized plasma are not always applicable here because the ions often have Larmor radii larger than the tube radius. The classical expectation that ions and electrons will diffuse across $\mathbf{B_0}$ at the same rate, so that no ambipolar electric field arises, is based on detailed momentum balance in each electron-ion collision. This balance does not hold if the ions cannot complete their cyclotron orbits within the tube. If the ions have Larmor radii $r_L$ much larger than tube radius $a$, however, one can assume that the ions exchange momentum with the wall sheaths much more than with the electron fluid. In that case, the ion fluid moves independently, like the neutrals, and the electrons diffuse by colliding with both the neutrals and the ions, at an effective collision rate $\nu_e = \nu_{eo} + \nu_{ei}$. This collision frequency can also be used in the parallel

direction. Thus, in weak fields the electron perpendicular and parallel diffusion and mobility coefficients are given by

Eq. (59) $$D_{\|e} = \frac{KT_e}{m\nu_e}, \quad \mu_{\|e} = \frac{e}{m\nu_e}, \quad D_{\perp e} = \frac{D_{\|e}}{1+\omega_c^2/\nu_e^2}, \quad \mu_{\perp e} = \frac{\mu_{\|e}}{1+\omega_c^2/\nu_e^2}.$$

In strong fields (defined below), Spitzer diffusion can be used, but in intermediate fields there is no simple formula.

The ions will diffuse mainly by resonant charge-exchange with neutrals of the same species. If the magnetic field is strong, Eq. (59) can also be used for the ions, with $\nu_e$ replaced by $\nu_{io}$. In weak fields, the ions can be considered to be unmagnetized; and in intermediate fields there is no simple formula. Whether the field is strong or weak depends on whether the ion Larmor radius is smaller or larger than the tube radius. In calculating $r_L$, one should use $T_e$ rather than $T_i$, because the ions are accelerated by the dc electric fields in the plasma, which are scaled to $T_e$. For instance, a 3-eV argon ion in a 100-G field has a Larmor radius of about 1 cm.

The fast primaries can also have large Larmor radii. For instance, a 200-eV electron in a 50-G field has a Larmor radius of about 1 cm. The diffusion of this component has the complications of ion diffusion, but the Coulomb cross section at these energies is much smaller than the ion charge-exchange cross section. The primaries behave more like collisionless particles which reach the walls fast and are lost by overcoming the Coulomb barrier there.

The classical transport mechanisms discussed above have the following limiting cases for diffusion across $\mathbf{B_0}$. For highly ionized discharges with magnetized ions, the classical diffusion coefficient is

Eq. (60) $$D_c = \eta_\perp n(KT_e + KT_i)/B^2,$$

where $\eta_\perp$ is the Spitzer resistivity (see Ref. 34). No ambipolar field is generated. In discharges with large ion Larmor radii, the electrons would be confined radially better than the ions, and a radial ambipolar field would be created to confine the ions. The resulting ambipolar diffusion coefficient is (Ref. 34)

Eq. (61) $$D_{a\perp} = \frac{\mu_{\perp i} D_{\perp e} + \mu_{\perp e} D_{\perp i}}{\mu_{\perp i} + \mu_{\perp e}} \approx D_{\perp e}\left(1 + \frac{T_i}{T_e}\right).$$

The ratio $T_i/T_e$ in Eq. (61) is usually small enough that the exact value of $T_i$ need not be known. If the ions are heated by collisions with electrons and are cooled by collisions with neutrals, calculations (Ref. 34) show that the equilibrium ion temperature is less than 0.1 eV. Direct measurements of the ion distribution function by laser-induced fluorescence give ion temperatures as high as 0.3 eV [Nakano et al. (71), Lieberman and Gottscho (65)], a somewhat higher value probably due to electric field oscillations in the plasma.

Diffusion along $\mathbf{B_0}$ would be ambipolar also, but with the electrons leaving faster than the ions, so that the ambipolar electric field along each line of force would be pointed away from the midplane. Thus, classical diffusion predicts a saddle-shaped potential distribution in which the plasma potential is concave across each diameter and convex along each line of force. Plasmas in strong magnetic fields, however, rarely exhibit classical diffusion, and, indeed, the predicted radial potential profile is not usually observed in helicon discharges. Fig. 33 shows a typical potential profile, which has a peak rather than a depression on the axis. The floating potential of a Langmuir probe often follows the density distribution, as if the electrons obeyed the Boltzmann relation

Eq. (62) $$n_e / n_0 = e^{eV/KT_e}$$

rather than the laws of cross-field diffusion. Perhaps undetectable high-frequency oscillations thermalize the electron population, as in the notorious Langmuir Paradox. Another possibility is that the number of poorly confined primary electrons is so large that their loss leaves the center of the plasma positive relative to the edge. These questions can be settled only after careful measurements of the plasma potential, which are difficult when a fast electron tail is present.

**Power balance.** A first attempt at modeling the power balance in a helicon discharge was made by Boswell (10). However, the rf power was only 180 W, below the threshold for a well established helicon wave, and the data could be fit only with an unreasonably low value of the energy expended in creating each ion-electron pair. More recently, Chen and Chevalier (34) have reconsidered the problem in the light of the transport mechanisms discussed above. Assuming that it takes, on the average, 200 eV to

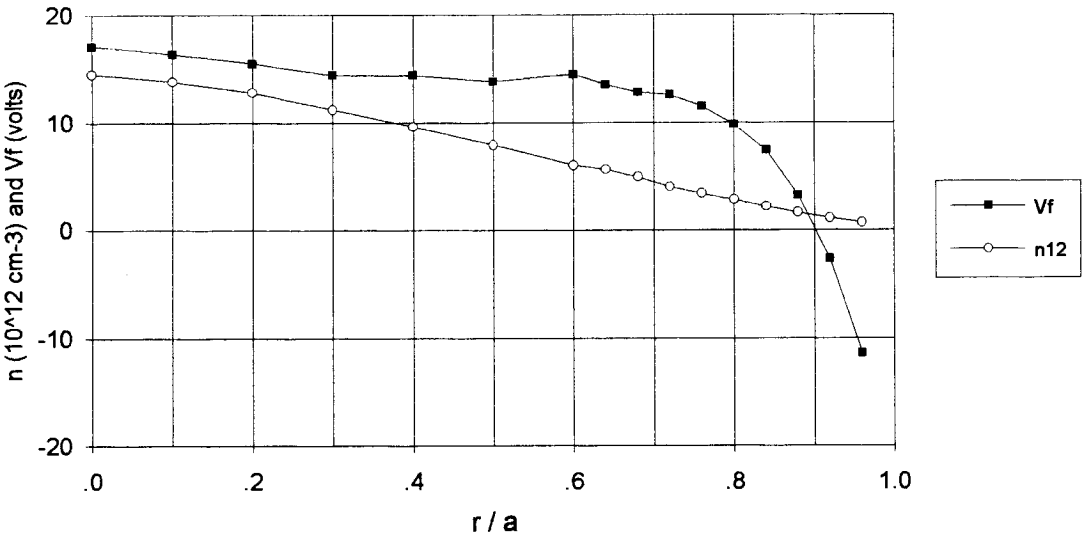


**Figure 33.** Radial profiles of density and probe floating potential in a 1 kG, 10-cm diameter argon helicon discharge (D.D. Blackwell, private communication).

ionize an atom, one can calculate the energy loss from escaping particles and compare this with the rf power absorbed in steady state. The loss in radiation is included in the 200 W figure. Since the diffusion equation is not separable in $r$ and $z$, axial and radial transport have been computed separately. For axial diffusion, $D_{a||}$ is used, and the boundary condition at the edge of the sheath on the endplates is that the ion flux is $nc_s$, where $c_s$ is the acoustic velocity. The resulting power loss is

Eq. (63) $$P \approx 3500(a^2 / L)_{cm} n_{13} \quad \text{W}.$$

In the radial direction, solution of the diffusion equation yields a density profile varying as the Bessel function $J_0(2.4r/a)$. Applying the diffusion coefficient given by Eqs. (61) and (59), one obtains for the radial power loss

Eq. (64) $$P = 2\left(\frac{n_{13}}{B_3}\right)^2 L_{cm} \quad \text{W}.$$

The radius $a$ cancels out here. Eqs. (63) and (64) are plotted vs density for L = 100 cm in Fig. 34. It is seen that axial losses depend on tube radius, while radial losses depend on magnetic field. For an $n \approx 2 \times 10^{13}$ cm$^{-3}$, $B_0 \approx 1000$ G, and a = 2.5 cm, the loss is about 1 kW for each process. This is in line with the total rf power of 2 kW in the experiment, but

the agreement may have been fortuitous because the details of the measured profiles were not considered.

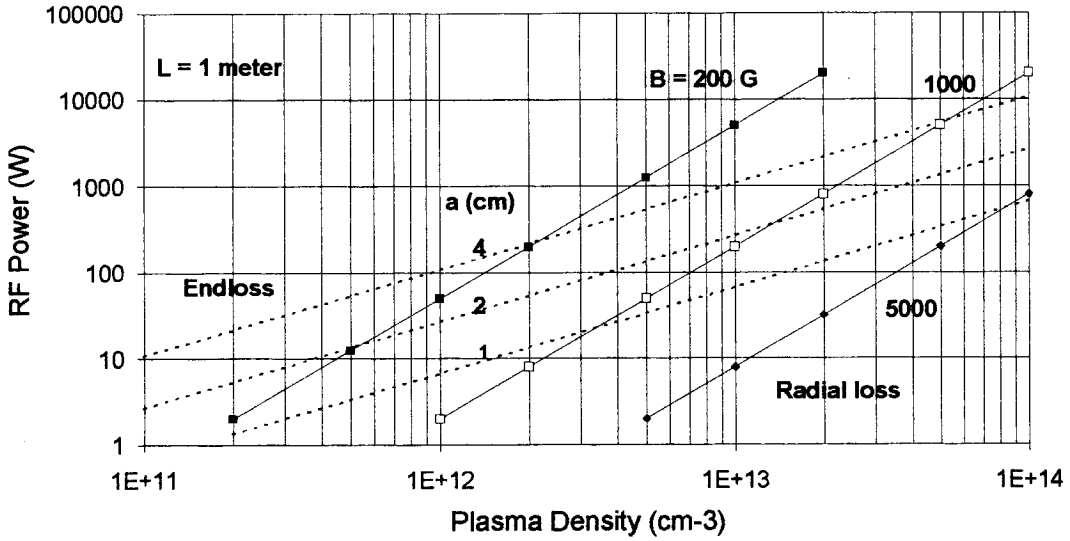


**Figure 34.** Rf power required to sustain a 1-m long discharge against radial losses (solid lines) and axial losses (dashed lines), computed separately, vs. plasma density, for various values of tube radius and magnetic field (Ref. 34).

**Gas feed.** A high-density helicon discharge is an efficient ion pump. To supply the particle losses corresponding to 2 kW of absorbed power and 200 eV for each ionization, $6 \times 10^{19}$ neutral atoms must be ionized per second. Since a tube 10 cm in diameter and 1 meter long contains $8 \times 10^{17}$ neutrals, these will be depleted in about 10 msec unless they are recycled. The process may proceed as follows. When a neutral atom migrates into the dense part of the plasma from the surrounding space, it has about a 10% probability of being ionized. Once it is ionized, it is accelerated up to the ion acoustic velocity by the presheath electric field. It therefore reaches the end of the tube at a much faster speed than its thermal speed as a neutral. When it hits the end of the chamber, the ion recombines and either goes into the pumpline there or slowly diffuses back toward the midplane at its thermal speed. Because the neutrals can reach the pump faster in the presence of plasma, the neutral pressure in the chamber reaches a steady state during the discharge which is lower than without plasma. The new equilibrium pressure can be reached in a few milliseconds. Figure 35 shows the plasma density in a helicon discharge during an rf pulse. The initial peak can be explained as the density with the full gas fill, and the following plateau as the density with the lower neutral pressure in the presence of plasma. The importance of ion pumping was first noticed by Boswell (10) in a Type A

device. Type B devices (Fig. 19) have a large plenum around the plasma for storage of gas and would be expected to suffer less from neutral depletion. Type C devices used for plasma processing can benefit from gas feed below the source, so that the processing chamber itself can act as a gas plenum.

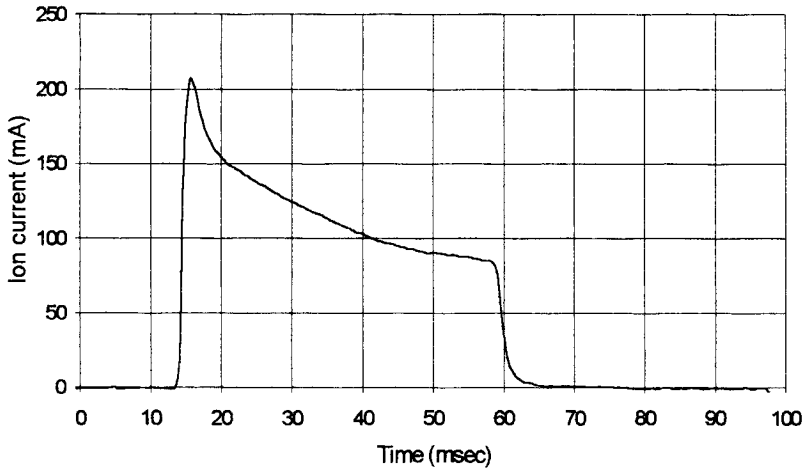


**Figure 35.** Density at r/a = 0.5 during an rf pulse, showing neutral depletion. Parameters were: a = 5 cm, B = 1 kG, p = 5 mTorr of argon, and 2.5 kW at 13.56 MHz (D.D. Blackwell, private communication).

### 4.3 Antenna design

Commonly used antennas are a half-wavelength long and shaped in one of the ways shown in Figs. 9 to 12. The length of the antenna, together with the rf frequency, determine the phase velocity to be excited, chosen to be resonant with either the thermal electrons or the fast primaries. However, a half-wavelength antenna will excite a broad range of $k$-values, and there is no guarantee that the wave will retain the same wavelength once it leaves the antenna region. Since no design code has been proved to have predictive reliability so far, empirical tests of antenna performance have been used. To achieve high density, Chen et al. (34) have varied the antenna length and shape, as shown in Figs. 36 and 37. In this case, an intermediate length of 12 cm, corresponding to a resonant energy of 120 eV, gave the highest density. If an antenna is too long, the phase

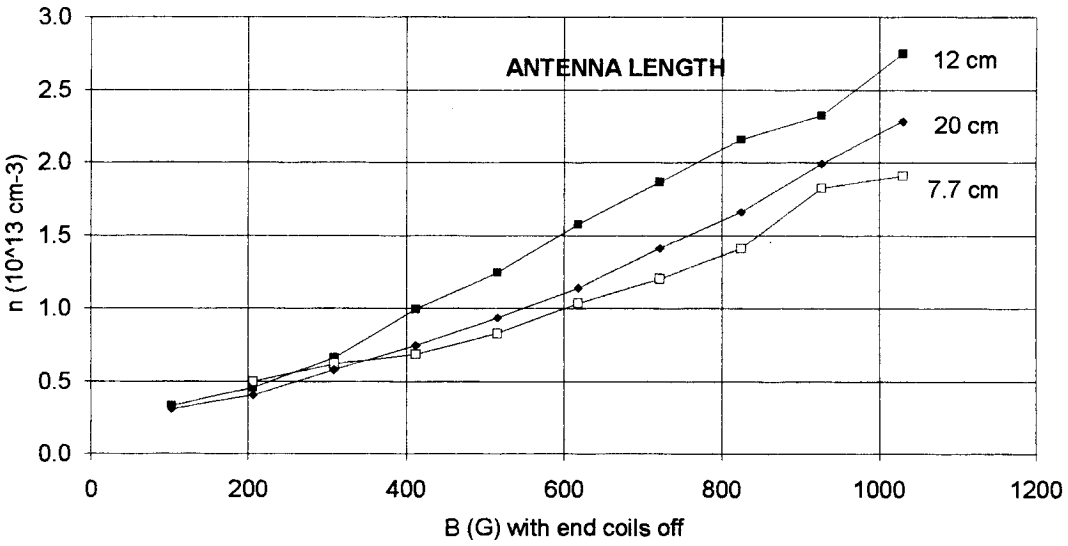


**Figure 36.** Peak density vs. magnetic field for Nagoya Type III antennas of different lengths (Ref. 34). Parameters were: a = 2 cm, p = 4 mTorr of argon, $P_{rf}$ = 2.2 kW at 27.12 MHz.

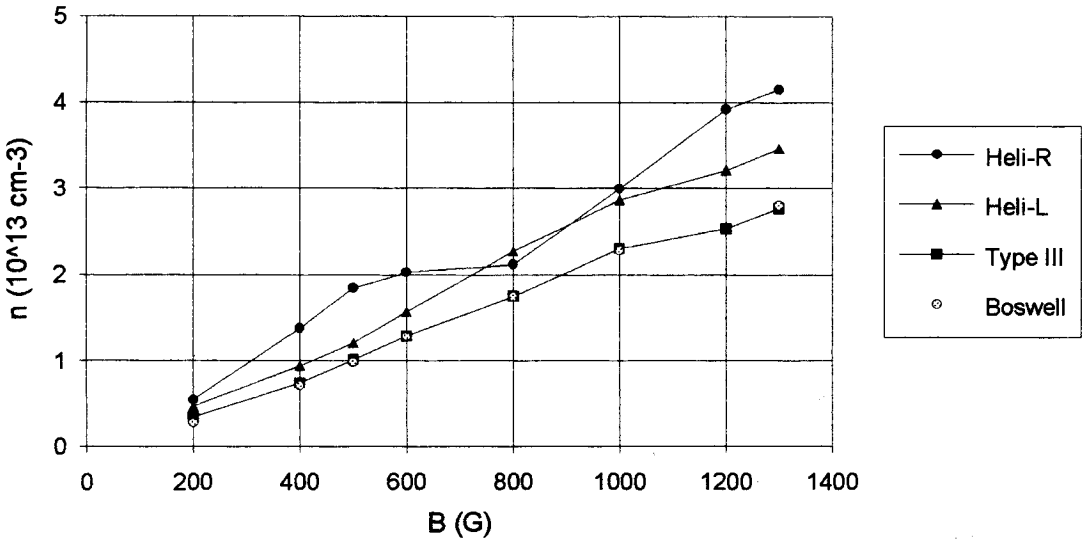


**Figure 37.** Peak density vs. magnetic field for four 12-cm long antennas of different designs (Ref. 34). Parameters were as in Fig. 36.

velocity is too high to be resonant with more than a few electrons; if the antenna is too short, coupling efficiency is low because the amplification factor in converting induced E-fields to space charge fields, proportional to $k_{\perp}^2/k_{||}^2$, is relatively small. In Fig. 37, the four antenna designs of Figs. 9-12 are compared under the same conditions. In this case, the Nagoya Type III and Boswell-type antennas gave the same results, while the helical

antennas, particularly the one designed to excite the m = +1 mode, gave higher peak densities. These results may not hold under other experimental conditions.

The antennas used by Campbell et al. (19, 18) have m = 0 symmetry and consist of two rings with current in opposite directions. The spacing between the rings and the placement of the leads have been optimized for plasma uniformity. These antennas were found to give more uniform density profiles than m = 1 antennas, even though the m = 0 mode has a peak in $B_z$ on the axis, while the m = 1 mode peaks off-axis. The coupling mechanism of the m = 0 mode is not yet understood. Capacitive coupling may play a role in increasing the edge density. Capacitive coupling may have been seen by Komori et al. (61) with an m = 1 antenna. There, it was shown that $n$ saturates with B and $P_{rf}$ at a value equal to the neutral density, indicating complete ionization, and that at fields below threshold, the density profile is hollow, indicating ionization by the near-field of the antenna. Antennas longer than a half-wavelength have not been tried, nor have bifilar helical antennas which can excite pure right- and left-hand circularly polarized modes. Optimization of antenna design has so far been done only by trial and error for each application.

### 4.4 Magnetic field shaping

"Helicon" sources used for plasma processing are generally short, with a nonuniform magnetic field in the source region and a multicusp or weak field in the processing chamber (see Fig. 20). In such devices, it is not clear whether or not helicon waves are excited at all. For weak gradients, one would expect helicon waves to adapt to the changing B-field by varying the axial wavelength. The basic dispersion relation given by Eqs. (13), (15), and (20) can be approximated by

Eq. (65)
$$\frac{3.83}{a} = \frac{\omega}{k}\frac{n_0 e \mu_0}{B_0},$$

where 3.83 has been taken as the lowest relevant Bessel root. Suppose the field lines diverge past the last magnetic field coil. The plasma tends to follow the field lines, so that the ratio $n_0/B_0$ remains approximately constant. Since the plasma radius $a$ increases, the dispersion relation requires $k$ to increase in proportion. The wavelength, therefore, can be expected to shorten in a diverging field. At some point the damping becomes so strong that the wave propagates no farther. This effect, called a "magnetic beach", was first

considered in connection with ion cyclotron waves in controlled fusion machines. This physical picture would not be expected to hold when the magnetic field is made to vary rapidly on the scale of an axial wavelength, as in most Type C devices.

One can also augment the current in the end coils of a solenoid so as to make a magnetic mirror to confine the plasma, as in fusion devices. This type of confinement is, however, not effective in low-temperature plasmas because of the electrons can scatter rapidly into the loss cone of the mirror.

To make contact between uniform-field theory and discharges in practical configurations, there have been a few controlled experiments to model the effect of field gradients [Chevalier and Chen (37)]. Instead of a simple decrease in helicon wavelength, the plasma was found to change dramatically when the field was made nonuniform in the antenna region. Fig. 38 shows the diverging field lines of a magnetic "cusp" field created by lowering the current in the end coils of a solenoid. In Fig. 39, one sees that the density on axis in the main part of the plasma increases as the end-coil current is decreased, and then reversed, to form a strongly diverging field; the density increases five-fold. The radial density profiles, shown in Fig. 40, indicate that the discharge is narrowed by the cusp field. Apparently, the diverging field lines that strike the chamber wall form a magnetic aperture limiter, effectively reducing the tube radius, because plasma is lost rapidly along these field lines. The magnetic limiter effect has also been noticed by Boswell et al. (15). The increase in density is, however, more than geometrical. The total number of particles integrated over the cross section increases by a factor of two, indicating that the ionization efficiency is increased. This may be related to the recovery of the rf energy which would otherwise be expended in exciting the "back wave" propagating from the antenna toward the end of the machine, or it may be due to the increased absorption in a "magnetic beach".

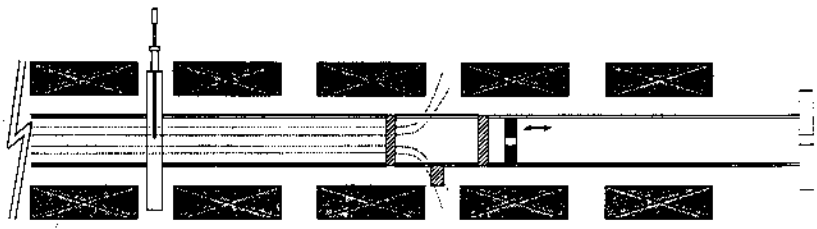

**Figure 38.** Schematic of experiment on helicon discharges with cusped fields and aperture limiters (Ref. 37). The field lines shown diverging in the region of the Nagoya Type III antenna are created when the two endcoils at the right are disconnected. A moveable aperture limiter is shown to the right of the antenna.

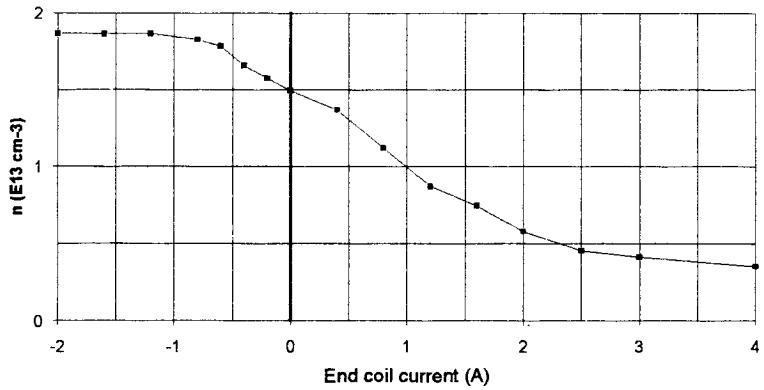


**Figure 39.** Increase in density on axis with decrease in end-coil current (Ref. 34). The current at the extreme right gives a uniform field.

To verify the magnetic aperture limiter idea, measurements were made with material aperture limiters, also shown in Fig. 38. Fig. 41 shows density profiles with a carbon limiter at various distances from the midplane of a Nagoya Type III antenna in a uniform magnetic field.

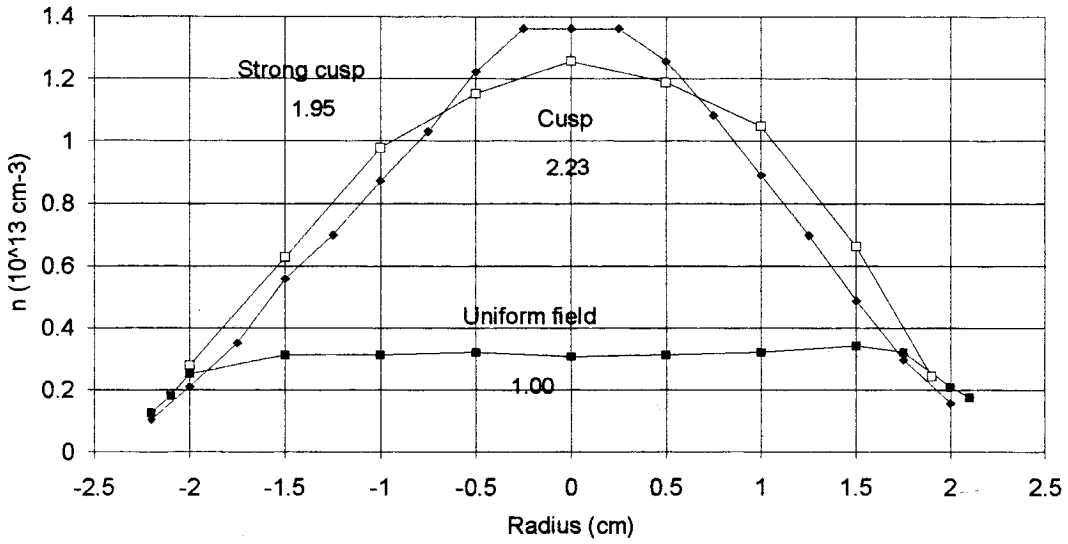


**Figure 40.** Radial density profiles in the uniform-field region of Fig. 36 for positive, zero, and negative end-coil currents corresponding to the right, center, and left regions of Fig. 37 (Ref. 37). The numbers on the curves are proportional to the integrated density in each cross section.

The material limiter enhances the peak density by about as much as a magnetic limiter does, as long as the limiter is behind the antenna and not between it and the main plasma

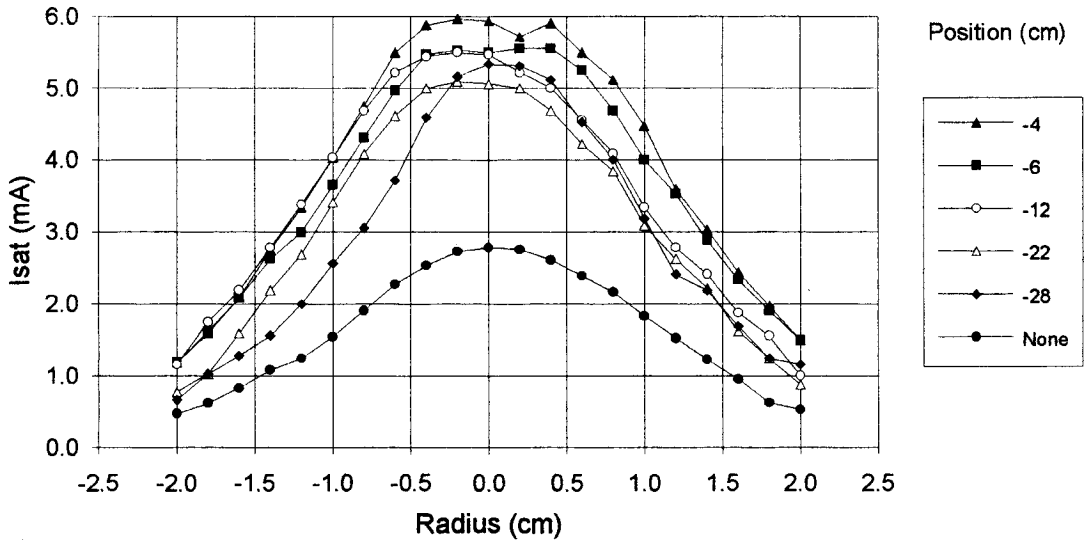


**Figure 41.** Radial density profiles with a 1.2-cm diameter carbon aperture limiter located at various distances from the midplane of a Nagoya Type III antenna. Negative values are positions between the antenna and the end of the vacuum tube, away from the midplane of the discharge (Refs. 84, 37).

chamber. The density increases as soon as the limiter is inserted, even far from the antenna. As the limiter is moved closer to the antenna, there is a small further increase in density. This sensitivity to position is not present if a cusp field is used, since the magnetic limiter, rather than the material limiter is then the active element. Furthermore, an increase in plasma density was observed even with a solid carbon block with no hole, as long as it was located just behind the antenna. There are several possible reasons for these strange results. First, when the carbon disk is in the neighborhood of the antenna, eddy currents could be excited in it, so that it becomes an internal antenna. This possibility was eliminated by using an insulating BN limiter of the same size; the density profiles were not changed. Second, the limiter could interfere with the flow of gas toward the pump, thus trapping the neutrals and maintaining a higher pressure in the presence of plasma. This possibility was eliminated by locating the pump at the far end of the tube, with no difference in the results. Third, ion bombardment of the limiter may introduce impurities in the plasma; but this does not explain the similarity with the cusp field results. Fourth, the limiter or solid block could act as a boundary to reflect helicon waves and eliminate the back wave. This is a likely explanation and points out the importance of avoiding excitation of helicons traveling in the undesired direction. Finally, the plasma potential is affected by the presence of the limiter; this may explain some of the anomalies at -6 cm

reported earlier (Ref. 37). The use of magnetic field shaping to flatten the density profile is also possible, but so far this has been done only by trial and error on Type C devices.

### 4.5 Matching networks

Antennas used to excite helicon waves present an inductive load to the rf power supply and are matched to it by either a capacitor network or a double-stub transmission line tuner. The latter is used at high frequencies when the capacitances become as small as stray capacitances. At the normal frequency of 13.56 MHz, two-capacitor networks in one of the following configurations are commonly used. Proper tuning is essential to obtaining efficient and reproducible discharges. Spurious minima in the reflected power can be seen when starting far from the ideal matching condition. After this is found manually, however, automatic tuning circuits can be used to maintain the match. Simple formulas for the loading capacitor $C_1$ and the tuning capacitor $C_2$ in the "standard" and "alternate" circuits shown in Fig. 42 have been given by Chen (29) in terms of the loaded resistance R and reactance X of the antenna and the angular frequency ω and output impedance $R_0$ of the power supply:

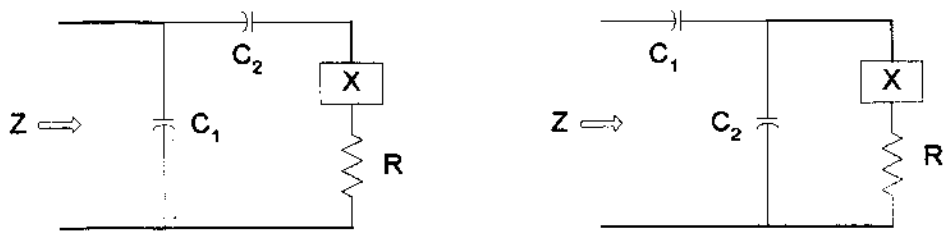


Standard circuit Alternate circuit

**Figure 42.** Schematics of simple capacitor matching circuits used in rf discharges.

Eq.(66) $$\omega C_1 = \frac{1}{2R}\left[1-\left(1-\frac{2R}{R_0}\right)^2\right]^{1/2}, \quad \omega C_2 = \left(X - \frac{1-R/R_0}{\omega C_1}\right)^{-1}$$ (Standard circuit)

Eq. (67) $$\omega C_1 = (R/R_0)/R_0 B, \quad \omega C_2 = (X - R_0 B)/(X^2 + R^2)$$ (Alternate circuit)

where $$R_0 B \equiv (R/R_0)^{1/2}\left[X^2 + R(R-R_0)\right]^{1/2} \quad .$$

Note that there is no solution for primarily capacitive loads (X < 0), such as an RIE discharge. Capacitor matching circuits are more suitable for inductive discharges. The length of cable connecting the matching circuit to the antenna should not be neglected. For a cable of length $kz$ radians and a load (antenna) impedance of $R_L - jX_L$, the impedance seen by the match circuit is

Eq. (68)
$$R = R_L / D, \qquad X = \left\{\left[1-\left(R_L^2 + X_L^2\right)\right]\sin kz \cos kz + X_L\left(\cos^2 kz - \sin^2 kz\right)\right\} / D$$

where $$D \equiv \left(\cos kz - X_L \sin kz\right)^2 + R_L^2 \sin^2 kz \quad .$$

It is common for the reflected power to be less than 1% of the incident power.

### 4.6 Semiconductor damage

As oxide gates in semiconductor devices become thinner than 10 nm, a problem arises in plasma processing because of the damage to these oxide layers caused by the acceleration of electrons into these layers by stray electric fields. Experiments by Fang and McVittie (47, 48) have shown that a plasma density gradient across a wafer can give rise to a corresponding potential gradient of sufficient magnitude to cause damage. Dalton and Sawin (40) have demonstrated experimentally that 15-V potentials can be generated by the **E** × **B** motions of electrons in a 100-G magnetic field parallel to the wafer. This result strongly indicates the necessity for locating the substrate in a field-free region.

The act of turning the plasma on and off itself induces dangerous fields. Chapman et al. (20) have reported that the potential of the wafer is initially 150 V relative to the plasma before it falls to below 30 eV as the discharge becomes fully established. Rapid pulsing of the plasma has been proposed to ameliorate microloading, which is the effect on etching of neighboring features, presumably due to the depletion of the reactive species. In fact, Boswell and Porteus (13) have shown that the overall etch rate is not reduced by pulsing even if the duty factor is only 20%. However, the damage that this would cause

could be large, and this technique may not be useful for delicate circuits. The study of damage by rf discharges is in its early stages.

### 4.7 Diagnostics

A large array of diagnostics exists which is common to all plasma processing tools. This includes microwave and infrared spectroscopy and interferometry, laser induced fluorescence, and optical spectroscopy, including actinometry. Helicon devices, however, have special conditions which affect the performance of probes. First, the presence of large radiofrequency fields distorts the I-V characteristics of Langmuir probes and requires careful cancellation. This problem does not occur in ECR devices, where the fields are in the GHz range, but is quite severe in rf sources. A large literature exists on the design of probes for measuring electron temperature and distribution functions in RIE discharges, and much of this information is also useful for helicon sources. It is well known that the rf makes the electron temperature appear higher and the floating potential lower than they really are. Sudit and Chen (85) have discussed this problem in connection with helicon discharges. Second, the magnetic field complicates the interpretation of probe curves. The electron current to the probe saturates at a relatively low value because the electrons drawn to the probe are not easily replaced by diffusion across the magnetic field, and the potential of the entire tube of force intercepted by the probe is changed. The space potential, therefore, cannot be obtained from the "knee" of the I-V curve, though sometimes the inflection point in this curve can be used. Emissive probes, if they can be made small, can in principle be used successfully for this application. Third, the high density of helicon discharges causes physical sputtering of the probe tip, which can change its collection area during an experiment. This can be minimized by using carbon tips (Ref. 85), by pulsing the plasma with small duty factor, or by fast mechanical sweeping of the probe across the plasma.

Magnetic probes for measuring the wave field suffer from electrostatic pickup of the rf field. Two methods have been used successfully to overcome this problem. One is to use a one turn loop made of thin coaxial cable (Ref. 66); this reduces the pickup to such a low level that the signal can be seen. The other is to use balanced multi-turn coils with transformer coupling to the coaxial cable; this increases the signal amplitude to overcome the pickup.

Other diagnostics for helicon discharges include the pitch-angle probe, which uses the strong magnetic field to distinguish the parallel from the perpendicular motion of ions [Lam and Hershkowitz (62)], and gridded velocity analyzers for measuring the parallel velocity distributions of both electrons and ions. A 6 $cm^2$ gridded analyzer was used by Boswell and Porteous (12) in 1986, and a particularly small, etched analyzer has recently been developed by Gibson et al. (51). Such analyzers, however, are subject to rf pickup and should be designed to operate in a helicon discharge environment.

## 5.0 HELICON REACTORS FOR ETCHING AND DEPOSITION

### 5.1 Commercial helicon reactors

Two reactors for semiconductor processing based on helicon sources have been made available commercially. Plasma and Materials Technologies, Inc. (PMT) of Chatsworth, California, manufactures the M=0 Reactive Ion etcher (MORI 200), with an antenna designed to excite the m = 0 helicon mode; and Lucas Signatone Corp. of Sunnyvale, California, offers the Vortex helicon source with m = 1 excitation. Techniques for gas and wafer handling, vacuum control, wafer chuck bias and cooling, 13.56 MHz rf power supplies, etc., are standard in the industry. These units differ in the design of the antennas and the magnetic field coils so as to produce uniform ion flux over a large area. Details of the source designs are generally proprietary; Figs. 43 and 44 show generic diagrams of these two systems.

The PMT source is particularly compact in its vertical dimensions; its performance has been reported by Campbell et al. (19, 18). The m = 0 antenna was found to give flatter density profiles in the source than m = 1 antennas. In the original experiments (Ref. 19), three magnetic coils were used to shape the field. When the plasma is made to expand toward the wafer chuck, the density, initially above $10^{12}$ $cm^{-3}$, drops a factor of four but becomes uniform over a 20 cm diameter. With 0.7 mTorr of argon, 600 G in the source, and 3 kW of rf power, the ion current impinging on the wafer was 110 $mA/cm^2$. With $SF_6$ gas, the density was about a factor of three lower, and the etch rate on polysilicon was measured to be 1.8 μm/min, with a 200:1 selectivity against $SiO_2$. More recent tests (Ref. 18) with the configuration of Fig. 43 employed lower magnetic fields of order 60-150 G, resulting in argon ion fluxes of order 50 $mA/cm^2$, uniform over a 20-cm

diam at 3 kW and 5 mTorr. In contrast to some of the results reported in the next section, the plasma properties were unaffected by rf bias power, up to 100W, applied to the chuck. Chlorine etching of polysilicon wafers patterned with 0.4 μm features yielded the results shown in Fig. 45. The etch rate of Si increases to 0.3 μm/min at 2 kW, increasing to 0.4 μm/min with 50 W of chuck power, while the $SiO_2$ rate decreases to zero, giving an essentially infinite selectivity. The selectivity against photoresist was of order 10. Uniformity was ±2% over 20 cm. Etching of aluminum by $Cl_2$ and $Cl_2$-$BCl_3$ gave a rate of 0.65 μm/min with 22:1 selectivity against oxide and 9:1 against photoresist. Etching of patterned tungsten with 3 mTorr of $SF_6$ and 1.5 kW of source power with 25-65 W of chuck power in a two-step process yielded a rate of 0.28 μm/min and a selectivity of 10:1 against oxide and 2:1 against photoresist.

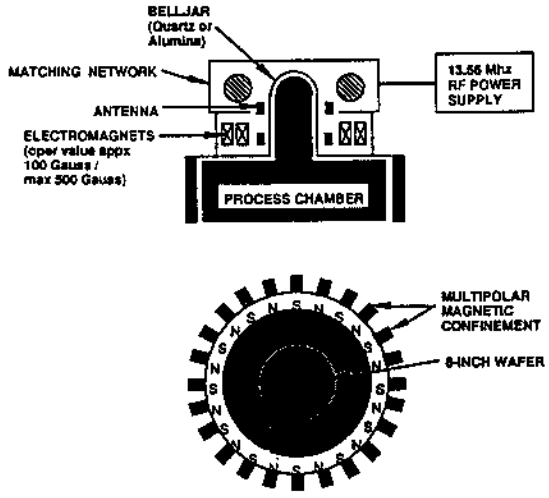


**Figure 43.** Schematic of the MORI etching tool of PMT, Inc., employing a 10-cm diam helicon source. The process chamber is 36 cm in diam, accommodating 20-cm diam wafers in a cooled chuck, located about 20 cm below the source (Ref. 18).

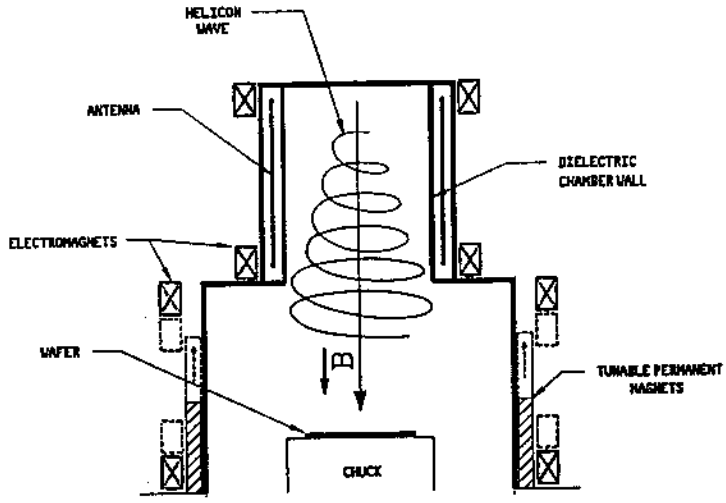


**Figure 44.** Schematic of the Vortex helicon etcher of Lucas Signatone Corp. (Ref. 20).

Similar performance in the Lucas source has been reported by Chapman et al. (20, 3). With source magnetic fields of 50-150 G and pressures of 1-10 mTorr, maximum ion fluxes of 150 mA/cm$^2$ and useful ion fluxes of 10 mA/cm$^2$, uniform to ±1% over 15 cm have been reported. Etch rates on photoresist, uniform to ±2%, reached 1.3 μm/min with

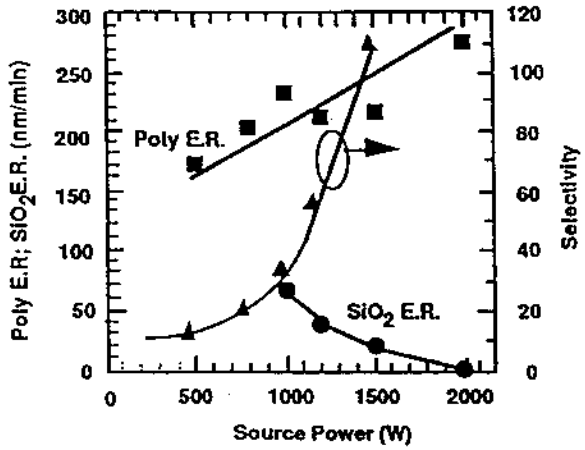


**Figure 45.** Etch rate and selectivity of $Cl_2$ on polysilicon and $SiO_2$ vs. rf power (Ref. 18).

an oxygen flow rate of 70 sccm at 2 mTorr, 2.5 kW of rf, and -100V of self-bias. The self-bias, or sheath drop at the wafer, is normally lower, in the 15-30 V range. Uniformity was measured with a tessellated probe (Refs. 3, 4), an array of hexagonal tiles in the wafer plane. Etch rate of HBr on polysilicon was measured to be 0.2 μm/min at 1 kW and 4.5 mTorr, with 50:1 selectivity against oxide and 15:1 against photoresist. Deposition of $SiO_2$ films was also reported, up to 10 μm thick at 0.2 μm/min with better than 5% uniformity.

### 5.2 Experiments with reactant gases

In addition to the experiments of Sec. 3, which emphasized the production of argon plasmas by helicon waves, more than a dozen papers have appeared regarding the performance of helicon reactors. Because of the large variety of substrates and radicals, these studies constitute a preliminary sampling of results, and no conclusions regarding any specific manufacturing process can be drawn. The studies of etching are divided into two groups: one by R.W. Boswell and collaborators in Australia, and the other by T. Shoji and collaborators in Japan.

In 1985, Boswell and Henry (11) reported interesting results on etching of masked Si and $SiO_2$ substrates in a pulsed $SF_6$ plasma at 7 mTorr and 100 G in a Type A machine. The Si etch rate increased discontinuously from 0.7 to 3 μm/min as the rf power was increased to 400 W, and then quickly saturated for powers >500 W. Apparently, the threshold for producing a high density was at 400 W, and the gas was completely

dissociated into atomic fluorine by 500 W, as indicated by the 634.8 nm line of fluorine. If the discharge is pulsed with constant 20% duty cycle, the polysilicon etch rate surprisingly increased by a factor of three when the pulse length was reduced from 1 sec to 1 msec. This was explained and modeled by assuming that etching continued between the pulses until the F atoms were lost by recombination on a 50 msec time scale. However, the etching in the absence of ions was isotropic. Etching of $SiO_2$, on the other hand, requires energetic ions, and its etch rate *increases* with pulse length and substrate bias. Thus, by using 1 msec pulses, selectivity could be increased to >100. Further experiments on the same device by Boswell and Porteous (13) showed that when a true helicon discharge is struck at fields of 500-800 G, atomic F is ionized to $F^+$, and all etching stops; hence, operation at 50-100 G, below the helicon threshold, is necessary. This paper gives a more detailed analysis of the pulsed etching process. At that time, the problem of damage by pulsing was not yet known. Ding et al. (44) have recently shown, for $CF_4/O_2$/A etching of Si and $SiO_2$ in ECR plasmas, that the etch rate depends only on the ion energy flux to the substrate, as long as the atomic fluorine density is above about $10^{12}$ $cm^{-3}$. This observation would seem to be at variance with the results of Boswell et al. with pulsed plasmas, in which the etch rate was independent of ion flux. Though the fluorine densities were about the same, the reported etch rates on Si differed by an order of magnitude (≈1.2 μm/min in Canberra vs. ≈0.12 μm/min in Wisconsin). At this time, we do not know which were the essential differences in the two experiments.

In 1989, Boswell, Perry, and Emami (15) studied the effect of multidipole magnetic confinement on plasma uniformity in $SF_6$. The Type C device had a 6-cm diam, 20 cm long source tube and a 30-cm diam, 40 cm long expansion chamber with 24 sets of 600-G permanent magnets on the surface. Though the density was lower than with a uniform magnetic field, the uniformity was greatly improved by the multidipoles. The plasma density contours over the substrate were mapped and showed uniformity to ±1.5% over a 15-cm diameter, with $SF_6$ ion currents of order 0.5 $mA/cm^2$. Perry and Boswell (73) also made a study of anisotropy of $Si/SiO_2$ etching by $SF_6$ in a reactor like that of Fig. 44, with a source chamber 15 cm in diam by 25 cm long and a target chamber 30 cm in diam by 30 cm long. At fields of 50-70 G, again below the helicon threshold, densities of 3-5 × $10^{11}$ $cm^{-3}$ were measured in the etching chamber with 3 mTorr of $SF_6$ and 500 W of rf power. Anisotropy at -160 V substrate bias improved with pressures under 1 mTorr, with etch rate decreasing to 0.7 μm/min and selectivity against $SiO_2$ to 5. Results with this device were summarized by Perry, Vender, and Boswell (74). These included a study of plasma breakdown and the change in electron velocity distribution during that

process. With multidipole confinement, uniform plasmas over a 20 cm diameter were produced with both $SF_6$ and $CHF_3$.

Kitagawa et al. (59) used a Type C device with separate solenoidal magnetic fields in the source and target chambers and an m = 1 helical antenna. The etch rate of $NF_3$ on Si, with 1 kW of rf power, a 600-G field, and a dc bias of -100 V varied strongly with pressure from 0.02 μm/min below 1 mTorr to 6 μm/ min at 5 mTorr, while the ion current varied in the opposite direction. The decrease in etch rate with increase in ion current was attributed to the high ionization efficiency, which destroyed the population of neutral fluorine. Since directional etching was achieved only at low pressure, it was found necessary, as in the Boswell experiments to decrease the magnetic field to 100 G, below the helicon threshold. The Si etch rate was approximately doubled by using a liquid-nitrogen cooled chuck, while the $SiO_2$ rate remained essentially the same. Results with $NF_3$ were best at 3 mTorr and 60 V bias, where the etch rate was 0.35 μm/min; and with $Cl_2$ at 1 mTorr with 150 V bias, where the rate was 0.15 μm/min. Uniformity of etching over a 14-cm diameter was achieved with 100 G in the source and 0 G in the etching chamber, and by increasing the source tube diameter from 6 to 15 cm. The etch rate then fell below 0.1 μm/min.

Etching of metals was tested in essentially the same apparatus by Jiwari et al. (54) using an m = 0 antenna. The magnetic field was 50 G in the source and 0 G in the stainless steel etching chamber. Typical conditions were 2 mTorr, 1.2 kW of rf, and 200 V bias. The m = 0 antenna produced uniform etching over a 20-cm diameter, with a slight peak near the walls. The presence of oxygen, coming from sputtering of the quartz vessel under the antenna, was found to dominate the etching of Al. Because of the formation of an oxide layer, pure $Cl_2$ could not etch Al at all. By adding 10% $BCl_3$, containing a reducing agent, and by using a bias voltage greater than 164 V, the etch rate was increased to 0.53 μm/min. Studies of the time behavior of etching, the variation with bias, and the concentrations of the neutral and ionized Cl and O species showed that Al etching could occur only after the chemical removal of a rapidly formed oxide layer.

Several papers by Shoji, Mieno, and Kadota (80, 81, 70) emphasized the use of helicon discharges for deposition. The apparatus was a modified Type B machine, with a 5-cm diam source tube feeding into a larger chamber with magnetic mirror coils. The magnetic field could be varied up to 2 kG, such that a region with B = 875 G could be produced within the mirror region. Thus, ECR heating with a 2.45-GHz, 5-kW source

could be applied as well as helicon excitation with a 1.5-kW, 3-30 MHz rf source. Deposition of amorphous carbon film was studied, using 2-mTorr argon plasmas with addition of 15% $CH_4$, $C_2H_2$, or CO. Electron densities were above $10^{13}$ $cm^{-3}$, and deposition rates reached 90 μm/hr, comparable to the rate normally obtained in high-pressure discharges. Although the CH radical density was higher for $CH_4$ than for $C_2H_2$, the latter gave a higher deposition rate, presumably because the rate is reduced by the presence of atomic hydrogen. By the same token, the deposition rate with CO was the highest of all, and it did not drop when the substrate cooling was turned off to increase the partial pressure of $H_2$, if any. The etching effect of hydrogen was confirmed by Mieno et al. (70) by showing that the deposition rate fell linearly with measured hydrogen partial pressure.

By using a gridded energy analyzer, Shoji et al. (80) were able to show that the population of fast electrons is continuously increased as the frequency, and hence the wave velocity, is increased from 9 to 19 MHz. The CH radical density showed a corresponding increase, saturating at 16 MHz. This was the first demonstration that the production of molecular species could be controlled by the making use of the helicon dispersion relation. In the same apparatus, Mieno et al. (69, 70) were able directly to compare the helicon discharge with an ECR discharge for deposition. At 1 mTorr under identical conditions, the two discharges produced the same deposition rate as a function of electron density. However, the helicon discharge produced more than four times higher density and was more controllable.

In addition to direct electron impact, production of reactive radicals can occur through the formation of metastables. As a first step in studying this process, Kadota and Shoji (55, 56) have used laser-induced fluorescence to measure the densities of metastable atoms in high-density He and Ne helicon discharges. The device was of Type B, operating at 1 kG, 1 kW, and 11 MHz in 2-msec pulses with a 1-50 Hz repetition rate. With 10-100 mTorr pressure, plasma densities were 0.6 and $2 \times 10^{13}$ for He and Ne, respectively. The metastable densities were higher in the afterglow than during the discharge, reaching 7.6 and $2.1 \times 10^{11}$ $cm^{-3}$ for He and Ne, respectively.

### 5.3 Summary and future applications

An ideal tool for plasma processing has to perform well according to the following four classical criteria:

1. Etch rate
2. Anisotropy
3. Uniformity
4. Selectivity.

The first two of these point to low-pressure, high-density plasmas, such as provided by ECR and RF discharges. In addition, we now have a number of other desirable features. The ion energy impinging on the substrate should be controllable, which means that the self-bias caused by the discharge should be small, or at least controllable; and an applied rf bias should not affect the plasma. The electron temperature and/or distribution function should be variable, so that the production of the reactive molecular species can be controlled. Device damage can be minimized the substrate is located in a region free from fast electrons, magnetic fields, and transverse electric fields. The discharge should introduce a modicum of heat, impurities, sputtering, and x-radiation. Oxygen released from the walls is useful for passivation, and this should be controllable by choice of wall material. Finally, the reactor should be small and economical. To satisfy all these requirements, an large number of adjustable parameters is required. The helicon source, including the low-field helicon-ECR branch, provides this flexibility of design because of the possible variations in magnitude and shape of the magnetic field, and the length and design of the antenna system. Indeed, experiments have shown that the normal, high-field branch of the helicon discharge is more suitable for deposition than for etching. The RIE discharge has comparatively little flexibility, and the ECR and RFI sources have invariable magnetic fields of 875 G and 0 G, respectively. Though the optimization process for helicon sources is a long one, those that already exist have impressive performance figures.

This chapter has emphasized the use of helicon discharges for production of ULSI circuits. However, there are many other possible applications. The high density and ionization efficiency of helicon sources make them also suitable for improved deposition of protective coatings and surface modification, and for reducing the sheath thickness in ion implantation processes. In the flat-panel display industry, the active matrix liquid crystal

display has a large potential market if the cost of producing thin-film transistors over large areas can be reduced. Since the low throughput is a large obstacle to low cost in present systems, increasing the etch rate with a high-density plasma source would be a logical step. Multiple sources could be combined to treat large areas uniformly. At the other end of the spectrum, a very small diameter but very high density plasma source is needed for accelerator applications. The requirements have been summarized by Chen (30). Though beat-wave accelerators require densities in the $10^{16}$-$10^{17}$ $cm^{-3}$ range, which is probably not possible with quasi-steady-state discharges, the wake-field accelerator and plasma lens are concepts which would require densities in the $10^{14}$-$10^{15}$ $cm^{-3}$ range, which should be accessible with focused helicon discharges if sufficient gas flow can be supplied. The possibilities for exploitation of helicon discharges are extensive, but their complexity requires a systematic study rather than a trial-and-error approach.

## ACKNOWLEDGMENTS

This work was supported by the Wisconsin Engineering Research Center on Plasma-Aided Manufacturing, by National Science Foundation Equipment Grant ECS 9212432, by the Lawrence Livermore Laboratory Plasma Physics Research Institute, and by the Semiconductor Research Corp., Contract No. 93-MJ-529. New results appearing here contain contributions from colleagues I.D. Sudit and G. Chevalier and students D. D. Blackwell and M. E. Light.

# BIBLIOGRAPHY


1. Abe, T., Nakazawa, S., Koshikawa, N., Sakawa, Y., and Shoji, T., Structure of energetic electrons in helicon plasma by using 2D emission intensity measurements, Proc. 2nd Int'l Conf. on Reactive Plasmas, Yokohama (1994).

2. Aigrain, P., Les "helicons" dans les semiconducteurs, Proc. Intl. Conf. on Semicond. Phys., Prague (Butterworths, London), p. 224 (1960).

3. Benjamin, N., Chapman, B., and Boswell, R., Progress of an advanced diffusion source plasma reactor, *Advanced Techniques for Integrated Circuit Processing, Proceedings of SPIE* 1392: 95 (1990).

4. Benjamin, N.M.P., Krieg, K.R., and Grover, G.T., Tessellated probe as an aid to process development, *Process Module Metrology, Control, and Clustering; Proceedings of SPIE* 1594: 153 (1991).

5. Bleven, H.A. and Christiansen, P.J., Propagation of helicon waves in a non-uniform plasma, *Aust. J. Phys.* 19: 501 (1966).

6. Bleven, H.A. and Christiansen, P.J., Helicon waves in a non-uniform plasma, *Plasma Phys.* 10: 799 (1968).

7. Bleven, H.A., Christiansen, P.J., and Davies, B., Effect of electron cyclotron resonance on helicon waves, *Phys. Rev. Lett. A* 28: 230 (1968).

8. Boswell, R.W., Plasma production using a standing helicon wave, *Phys. Lett. A* 33: 457 (1970).

9. Boswell, R.W., Effect of boundary conditions on radial mode structure of whistlers, *J. Plasma Phys.* 31: 197 (1984).

10. Boswell, R.W., Very efficient plasma generation by whistler waves near the lower hybrid frequency, *Plasma Phys. and Controlled Fusion* 26: 1147 (1984).

11. Boswell, R.W. and Henry, D., Pulsed high rate plasma etching with variable Si/SiO2 selectivity and variable Si etch profiles, *Appl. Phys. Lett.* 47: 1095 (1985).

12. Boswell, R.W. and Porteus, R.K., Large volume, high density rf inductively coupled plasma, *Appl. Phys. Lett.* 50: 1130 (1987).

13. Boswell, R.W. and Porteus, R.K., Etching in a pulsed plasma, *J. Appl. Phys.* 62: 3123 (1987).

14. Boswell, R.W. and Vender, D., Simulation of pulsed electropositive and electronegative plasmas, *IEEE Trans. on Plasma Science* 19: 141 (1991).

15. Boswell, R.W., Perry, A.J., and Emami. M., Multipole confined diffusion plasma produced by 13.56 MHz electrodeless source, *J. Vac. Sci. Technol. A* 7: 3345 (1989).

16. Boswell, R.W., Porteus, R.K., Prytz, A., Bouchoule, A., and Ranson, P., Some features of rf excited fully ionized low pressure argon plasma, *Phys. Lett. A* 91: 163 (1982).

17. Bowers, R., Legendy, C., and Rose, F.E., Oscillatory galvanomagnetic effect in metallic sodium, *Phys. Rev. Lett.* 7: 339 (1961).

18. Campbell, G.A., de Chambrier, A., Mendoza, F., Parker, N.W., Pearson, D.I.C., Tokunaga, K., Tsukada, T., Mashiro, S., and Nogami, H., MORI, a high density rf plasma source for etching of polysilicon and metal films on wafers, *Proceedings of the Society of Photo-Optical Instrumentation Engineers* 1803: 226 (1992).

19. Campbell, G.A., Pearson, D.I.C., and de Chambrier, A.P., High ion flux rf source for ion assisted processes, Proc. 33rd Annual Techn. Conf., Society of Vacuum Coaters (1990).

20. Chapman, B., Benjamin, N., van Os, C.F.A., Boswell, R.W., and Perry, A.J., Plasma dry processing in the helicon reactor, 12th Symposium on Dry Process, Denki-Gakkai, Tokyo (1991).

21. Charles, C., Ion energy distribution functions in a multipole confined argon plasma diffusing from a 13.56-MHz helicon source, *J. Vac. Sci. Technol. A* 11: 157 (1993).

22. Chen, F.F., Radiofrequency field enhancement near ion gyroresonance, TRW Report Task II-3552 (1981) (unpublished).

23. Chen, F.F., Landau damping of helicon waves, Australian National Univ. Report ANU-PRL IR 85/12 (1985) (unpublished).

24. Chen, F.F., Helicon wave plasma sources, *Proceedings of the Int'l Conf. on Plasma Physics, Kiev, USSR* 2: 1378 (World Scientific, Singagore) (1987).

25. Chen, F.F., RF production of high density plasmas for accelerators, *Lasers and Particle Beams* 7: 551 (1989).

26. Chen, F.F., Helicon waves at low magnetic fields, UCLA Report PPG-1270 (1989) (unpublished).

27. Chen, F.F., Plasma ionization by helicon waves, *Plasma Phys. and Controlled Fusion* 33: 339 (1991).

28. Chen, F.F., Electron runaway in RF discharges, Plasma Science Center, Nagoya Univ., Report PSC-25 (1992).

29. Chen, F.F., Capacitor tuning circuits for inductive loads, UCLA Report PPG-1401 (unpublished) (1992).

30. Chen, F.F. , Excitation of large amplitude plasma waves, *Physica Scripta* T30: 14 (1990).

31. Chen, F.F. and Decker, C.D., Plane-polarized whistler waves, *Bull. Amer. Phys. Soc.* 35: 2101 (1990).

32. Chen, F.F. and Decker, C.D., Electron acceleration in helicon sources, *Plasma Phys. and Controlled Fusion* 34: 635 (1992).

33. Chen, F.F. and Chevalier, G., RF production of long, dense plasma columns, Int'l Conf. on Plasma Physics III, 1701 (Inst. for Ion Physics, Univ. of Innsbruck, A-6020 Innstruck, Austria) (1992).

34. Chen, F.F. and Chevalier, G., Experiments on helicon plasma sources, *J. Vac. Sci. Technol. A* 10: 1389 (1992).

35. Chen, F.F., Hsieh, M.J., and Light, M., Helicon waves in a nonuniform plasma, *Plasma Sources Science and Technology* : (to be published) (1994).

36. Chen. F.F. and Chevalier, G., Diagnostics of rf plasmas for semiconductor etching, *Calif. Microelec. Innov. and Computer Research Opportunities (MICRO) Project Reports* 1991-92: 348 (1993).

37. Chevalier, G. and Chen, F.F., Experimental modeling of inductive discharges, *J. Vac. Sci. Technol. A* 11: 1165 (1993).

38. Christopoulos, C., Boswell, R.W., and Christiansen, P.J., Measurements of spatial cyclotron damping in a uniform magnetic field, *Phys. Lett. A* 47: 239 (1974).

39. Cui, C., and Boswell, R.W., Role of excitation frequency in a low-pressure, inductively coupled radio-frequency, magnetized plasma, *Appl. Phys. Lett.* 63: 2331 (1993).

40. Dalton, T.J. and Sawin, H.H., Spatially resolved plasma and wafer surface potential measurements, Abstract RA-4, Gaseous Electronics Conf., Montreal, Canada (1993).

41. Davies, B.J., Helicon wave propagation: effect of electron inertia, *J. Plasma Phys.* 4: 43 (1970).

42. Davies, B.J. and Christiansen, P.J. , Helicon waves in a gaseous plasma, *Plasma Phys.* 11: 987 (1969).

43. Decker, C.D. and Chen, F.F., High density ECR source at 30 MHz, *Bull. Amer. Phys. Soc.* 35: 2102 (1990).

44. Ding, J., Jenq, J.-S., Kim, G.-H., Maynard, H.L., Hamers, J.S., Hershkowitz, N., and Taylor, J.W., Etching rate characterization of $SiO_2$ and Si using ion energy flux and atomic fluorine density in a $CF_4/O_2/Ar$ electron cyclotron resonance plasma, *J. Vac. Sci. Technol. A* 11: 1283 (1993).

45. Druyvesteyn, M.J. and Penning, F.M., Mechanism of electric discharges in gases of low pressure, *Rev. Mod. Phys.* 12: 87 (1940).

46. Ellingboe, A.R., Boswell, R.W., Booth, J.P., and Sadeghi, N., Time and spatially resolved optical emission in a helicon reactor, Abstract CA-5, Gaseous Electronics Conf., Montreal, Canada (1993).

47. Fang, S. and McVittie, J.P., Thin -oxide damage from gate charging during plasma processing, *IEEE Electron Device Lett.* 13: 288 (1992).

48. Fang, S. and McVittie, J.P., A model and experiments for thin oxide damage from wafer charging in magnetron plasmas, *IEEE Electron Device Lett.* 13: 347 (1992).

49. Ferrari, R.L. and Klozenberg, J.P. (1968), Dispersion and attenuation of helicon waves in a cylindrical plasma-filled waveguide, *J. Plasma Phys.* 2: 283 (1968).

50. Giapis, K.P., Sadeghi, N., Margot, J., Gottscho, R.A., and Lee, T.C. J., Limits to ion energy control in high density glow discharges: measurement of absolute metastable ion concentrations, *J. Appl. Phys.* 73: 7188 (1993).

51. Gibson, G.W., Jr., Blayo, N., Ibbotson, D., Lee, J.T.C., Sawin, H.H., and Tepermeister, I., Side by side comparison of ion energy distribution functions for helicon and multipolar ECR sources in an HBr discharge, Abstract AA-1, Gaseous Electronics Conf., Montreal, Canada (1993).

52. Harding, G.N. and Thonemann, P.C., A study of helicon waves in indium, *Proc. Phys. Soc.* 85: 317 (1965).

53. Harvey, B.M. and Lashmore-Davies, C.N., The absorption mechanisms of whistler waves in cool, dense, cylindrically bounded plasmas, *Phys. Fluids B* 5: 3864 (1993).

54. Jiwari, N., Iwasawa, H., Narai, A., Sakaue, H., Shindo, H., Shoji, T., and Horike, Y., Al etching characteristics employing helicon wave plasma, *Japan J. Appl. Phys.* 32: 3019 (1993).

55. Kadota, K. and Shoji, T., Efficient production of metastable rare gas atoms by recombining plasma of high density, Proc. Int'l Seminar on Reactive Plasmas, Nagoya, Japan, p.169 (1991).

56. Kadota, K. and Shoji, T., Population density distributions of excited rare gas atoms in high density whistler plasma, Proc. 20th Int'l Conf. on Phen. in Ionized Gases, Pisa, Italy, p. 1430 (1991).

57. Kadota, K., Konno, Y., Aoto, K., Shoji, T., and Sato, T., Density measurements of O-atoms in helicon wave oxygen discharge by two-photon laser-induced fluorescence, Proc. 2nd Int'l Conf. on Reactive Plasmas, Yokohama (1994).

58. Kamo, T., Mieno, T., Shoji, T., and Kadota, K., Measurement of ion fractions in helicon wave $CF_4$ plasma by TOF mass analysis, Proc. 2nd Int'l Conf. on Reactive Plasmas, Yokohama (1994).

59. Kitagawa, H., Tsunoda, A., Shindo, H., and Horiike, Y., Etching characteristics in helicon wave plasma, *Plasma Sources Science and Technology* 2: 11 (1993).

60. Klozenberg, J.P., McNamara, B., and Thonemann, P.C. , Dispersion and attenuation of helicon waves in a uniform cylindrical plasma, *J. Fluid Mech.* 21: 545 (1965).

61. Komori, A., Shoji, T., Miyamoto, K., Kawai, J., and Kawai, Y., Helicon waves and efficient plasma production, *Phys. Fluids B* 3: 893 (1991).

62. Lam, S.W. and Hershowitz, N., A new ion pitch-angle diagnostic for magnetized plasmas, (preprint) (1993).

63. Lawler, J.E., Parker, G.J., and Hitchon, W.N.G., Radiation trapping simulations using the propagator function method with complete frequency redistribution, Abstract PB-2, Gaseous Electronics Conf., Montreal, Canada (1993).

64. Lehane, J.A. and Thonemann, P.C., Experimental study of helicon wave propagation in a gaseous plasma, *Proc. Phys. Soc.* 85: 301 (1965).

65. Lieberman, M.A. and Gottscho, R.A., Design of high density plasma sources for materials processing, in : Physics of Thin Films, Academic Prsss (1994).

66. Light, M. and Chen, F.F., Measurements of helicon field patterns, *Bull. Amer. Phys. Soc.* 38: 1897 (1993).

67. Limpaecher, R. and MacKenzie, K.R., Magnetic multipole containment of large uniform collisionless quiescent plasmas, *Rev. Sci. Instrum.* 44: 726 (1973).

68. Loewenhardt, P.K., Blackwell, B.D., Boswell, R.W., Conway, G.D., and Hamberger, S.M., Plasma production in a toroidal heliac by helicon waves, *Phys. Rev. Lett.* 67: 2792 (1991).

69. Mieno, T., Shoji, T., and Kadota, K., Control of hydrocarbon radicals and film deposition by using a whistler wave discharge in range of radio frequency, *Appl. Phys. Lett.* 59: 2675 (1991).

70. Mieno, T., Shoji, T., and Kadota, K., Control of hydrocarbon radicals and amorphous carbon film deposition by means of rf whistler wave discharge, *J. Appl. Phys.* 31: 1879 (1992).

71. Nakano, T., Gottscho, R.A., Sadeghi, N., Trevor, D.J., Boswell., R.W., Perry, A.J., Lee, T.C., Giapis, K.P., and Margot, J., Helicon wave excited plasmas, *Oyo Buturi (Japan Soc. of Appl. Phys.)* 61: 711 (1992).

72. Okamura, S., Adati, K., Aoki, T., Baker, D.R., Fujita, H., Garner, H.R., Hattori, K., Hidekuma, S., Kawamoto, T., Kumazawa, R., Okubo, Y., and Sato, T., Plasma production with potating ion cyclotron waves excited by Nagoya Type-III antennas in RFC-XX, *Nuclear Fusion* 26: 1491 (1986).

73. Perry, A.J. and Boswell, R.W., Fast anisotropic etching of silicon in an inductively coupled plasma reactor, *Appl. Phys. Lett.* 55: 148 (1989).

74. Perry, A.J., Vender, D., and Boswell, R.W., Application of the helicon source to plasma processing, *J. Vac. Sci. Technol. B* 9: 310 (1991).

75. Rose, F.E., Taylor, M.T. and Bowers, R., Low-frequency magneto-plasma resonances in sodium, *Phys. Rev.* 127: 1122 (1962).

76. Sato, T., Okamura, S., Adati, K., Aoki, T., Baker, D.R., Fujita, H., Garner, H.R., Hattori, K., Hidekuma, S., Kawamoto, T., Kumazawa, R., Okubo, Y., and Uchino, K., Buildup and sustainment of $10^{13}$ $cm^{-3}$ plasma by ICRF in RFC-XX, Nagoya Univ. Inst. of Plasma Physics Report IPPJ-653 (1983).

77. Shoji, T., , IPPJ Annual Review, Nagoya University, Japan, p. 67 (1986).

78. Shoji, T., , IPPJ Annual Review, Nagoya University, Japan, p. 63 (1987).

79. Shoji, T., , IPPJ Annual Review, Nagoya University, Japan, p. 83 (1988).

80. Shoji, T., Mieno, T., and Kadota, K., Control of energy distribution of electrons and hydrocarbon film deposition by whistler wave discharge, Proc. Int'l Seminar on Reactive Plasmas, Nagoya, Japan, p. 377 (1991).

81. Shoji, T., Mieno, T., and Kadota, K., Production of hydrocarbon radical and film deposition in high density rf discharge, Proc. 20th Int'l Conf. on Phen. in Ionized Gases, Pisa, Italy, p. 1430 (1991).

82. Shoji, T., Sakawa, Y., Nakazawa, S., Kadota, K, and Sato, T., Plasma production by helicon waves, *Plasma Sources Science and Technology* 2: 5 (1993).

83. Shoucri, M.M., Helicon waves in cylindrical plasma columns, *Plasma Physics* 11: 1017 (1969).

84. Sudit, I.D., (unpublished) (1993).

85. Sudit, I.D. and Chen, F.F., RF compensated probes for high-density discharges, *Plasma Sources Science and Technology* (to be published) (1994).

86. Sudit, I.D. and Chen, F.F., A nonsingular helicon wave equation for a nonuniform plasma, *Plasma Sources Science and Technology* (to be published) (1994).

87. Wamsley, R.C., Mitsuhashi, K., and Lawler, J.E., Ionization balance in the negative glow of a Hg-Ar hot-cathode discharge, *Phys. Rev. E* 47: 3540 (1993).

88. Watari, T., Hatori, T., Kumazawa, R., Hidekuma, S., Aoki, T., Kawamoto, T., Inutake, M., Hiroe, S., Nishizawa, A., Adati, K., Sato, T., Watanabe, T., Obayashi, H., and Takayama, K., Radio-frequency plugging of a high density plasma, *Phys. Fluids* 21: 2076 (1978).

89. Woods, L.C., Hydromagnetic waves in a cylindrical plasma, *J. Fluid Mech.* 13: 570 (1962).

90. Woods, L.C., On the boundary conditions at an insulating wall for hydromagnetic waves in a cylindrical plasma, *J. Fluid Mech.* 18: 401 (1964).

91. Zhu, P. and Boswell, R.W., ArII laser generated by Landau damping of whistler waves at the lower hybrid frequency, *Phys. Rev. Lett.* 63: 2805 (1989).

92. Zhu, P. and Boswell, R.W., Observation of nonthermal electron tails in an RF-excited argon magnetoplasma, *Phys. Fluids B* 3: 869 (1991).